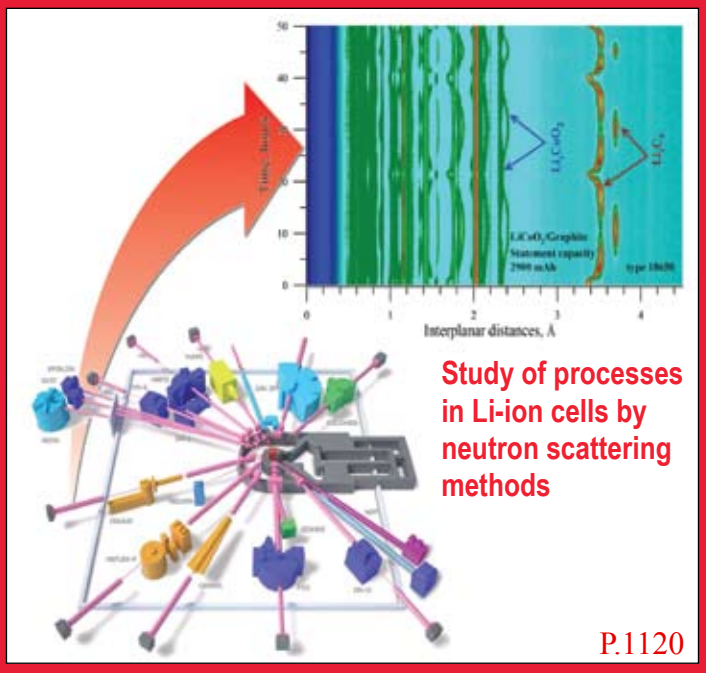
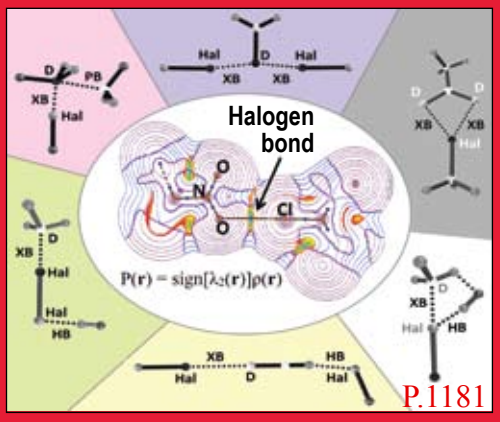
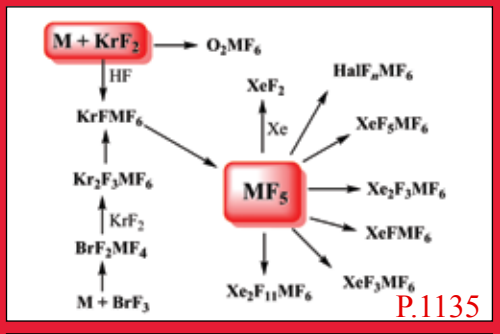
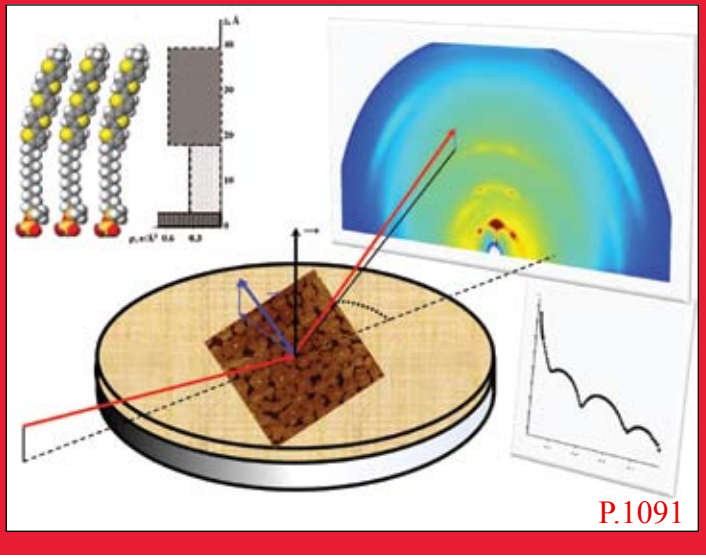
ISSN 0036-021X

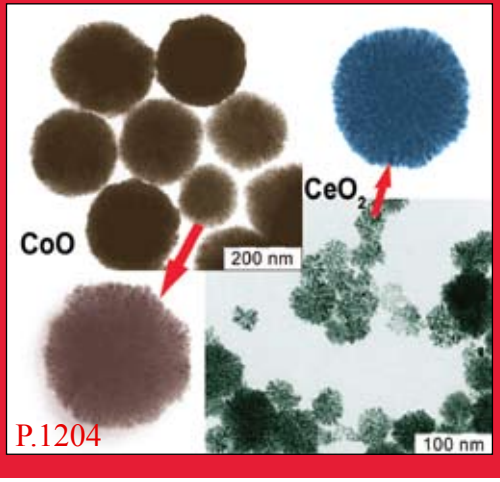
Russian Chemical Reviews











Reviews on current topics in chemistry

International Year of Crystallography

Volume 83 2014 Number 12

Russian Chemical Reviews **83** (12) 1091 – 1119 (2014) © 2014 Russian Academy of Sciences and Turpion Ltd

DOI 10.1070/RCR4485

Modern approaches to investigation of thin films and monolayers: X-ray reflectivity, grazing-incidence X-ray scattering and X-ray standing waves

M A Shcherbina,[a, b] S N Chvalun,[b, c] S A Ponomarenko,[a] M V Kovalchuk [c]

[a] *Enikolopov Institute of Synthetic Polymer Materials, Russian Academy of Sciences ul. Profsoyuznaya 70, 117393 Moscow, Russian Federation*
[b] *Moscow Institute of Physics and Technology (State University) Institutskii per. 5, 141707 Dolgoprudnyi, Moscow Region, Russian Federation*
[c] *National Research Centre 'Kurchatov Institute' pl. Kurchatova 1, 123098 Moscow, Russian Federation*

The review concerns modern experimental methods of structure determination of thin films of different nature. The methods are based on total reflection of X-rays from the surface and include X-ray reflectivity, grazing-incidence X-ray scattering and X-ray standing waves. Their potential is exemplified by the investigations of various organic macromolecular systems that exhibit the properties of semiconductors and are thought to be promising as thin-film transistors, light-emitting diodes and photovoltaic cells. It is shown that combination of the title methods enable high-precision investigations of the structure of thin-film materials and structure formation in them, *i.e.*, it is possible to obtain information necessary for improvement of the operating efficiency of elements of organic electronic devices.
The bibliography includes 92 references.

Contents

I. Introduction 1091
II. Methods of preparation and investigation of thin films 1092
III. Oligothiophene derivatives and their application in organic electronics 1106

M A Shcherbina Candidate of Physical and Mathematical Sciences, Leading Researcher at the ISPM RAS, Assistant Professor, Department of Molecular and Chemical Physics of MIPT.
Telephone (8-495) 332 58 20, e-mail: shcherbina@ispm.ru
S N Chvalun Doctor of Chemical Sciences, Head of Department of Crystallography and Materials Science, NBIC Centre, NRC 'Kurchatov Institute', Professor of the same Department.
Telephone (7-499) 196 78 96, e-mail: serge@ispm.ru
S A Ponomarenko Corresponding Member of the Russsian Academy of Sciences, Doctor of Chemical Sciences, Head of Laboratory for Functional Materials for Organic Electronics and Photonics of the ISPM RAS.
Telephone (7-495) 332 58 79, e-mail: ponomarenko@ispm.ru
M V Kovalchuk Corresponding Member of the Russsian Academy of Sciences, Doctor of Physical and Mathematical Sciences, Director of the NRC 'Kurchatov Institute'.
Telephone (7-499) 196 95 39, e-mail: nrcki@nrcki.ru
Current research interests: structure and properties of polymers and composites, X-ray diffraction, crystallization, self-assembly and self-organization, biodegradable polymers.

Received 15 July 2014
Uspekhi Khimii **83** (12) 1091 – 1119 (2014); translated by A M Raevskiy

I. Introduction

Modification of the surface of various materials to impart specific properties to them by depositing thin-film coatings is widely used in modern technologies. The properties and operating characteristics of the modified coatings are first of all determined by their structure. Elucidation of the structure of thin films and their transformations in the course of synthesis and under operating conditions is topical from the standpoint of both basic research and practice.

The available experimental methods based on reflection of X-ray radiation from the surface of thin films, monomolecular and multimolecular layers (X-ray reflectivity, grazing-incidence X-ray scattering, X-ray standing waves) make it possible to study the structure of these systems and mechanisms of transformation in the course of processing and operation. This offers prospects for targeted design of complex-architecture molecular systems with a specified set of unique physicomechanical, optical and chemical properties. Progress in these methods is intimately connected with the design of powerful sources of X-ray radiation, especially X-ray synchrotron radiation, and with the design of software for processing large data arrays using a complex

mathematical formalism to describe the interaction of radiation with matter.

This review is devoted to the main modern methods of investigation of the structure of thin-film mono- and multimolecular coatings prepared in different manner, namely, by centrifugation, cast, dipping, vapour phase deposition and self-assembly. The emphasis is placed on X-ray reflectivity, grazing-incidence X-ray scattering and X-ray standing waves.

II. Methods of preparation and investigation of thin films

II.1. Methods of preparation

There is a variety of methods for preparation of thin-film coatings. Among them, the Langmuir – Blodgett (LB) and Langmuir – Schaefer (LS) techniques are most widely used in laboratory practice because they allow one to specify and control the film thickness and to predict the film structure.[1] These methods are applicable in the case of amphiphilic low-molecular-mass and high-molecular-mass compounds (often, surfactants). A preliminary step involves the formation of a 2D ordered monomolecular layer (monolayer) on the surface of a liquid subphase; then, the monolayer is transferred to a solid substrate.[2] The quality of the thin-film coating transferred to the substrate depends on many factors including the mechanism of formation and the thermodynamic stability of the monolayer, the substrate material, the transfer technique, *etc.*[3,4]

Monolayers at the air/liquid interface are formed as a result of adsorption of surfactants that are soluble in the subphase (Gibbs monolayer) or after spreading of dilute solutions of insoluble surfactants and evaporation of organic solvent (Langmuir monolayer).[5] In the case of free spreading of a Langmuir monolayer on the subphase surface, the entropy (S_s) is given by[6]

$$S_s = \left(\frac{\partial S}{\partial A_f}\right)_{T,\Sigma} = -\left(\frac{\partial^2 F}{\partial T \partial A_f}\right)_{\Sigma} = -\left(\frac{\partial \pi}{\partial T}\right)_{A_f,\Sigma} \quad (1)$$

where S is entropy, A_f is the surface area of the film, T is temperature, $\Sigma = A_f + A_w$, A_w is the water surface area, F is the free energy, π is the surface pressure equal to the surface tension difference between the neat solvent (γ_0) and the film-coated solvent (γ_f)

$$\pi = \gamma_0 - \gamma_f$$

Physically, the surface pressure manifests itself as a force acting on the unit length of the barrier separating two surfaces.[7] To characterize the phase behaviour of an amphiphilic compound in the monolayer compression – tension mode, one should plot the dependence of the surface pressure on the surface area per molecule (A) at constant temperature, *i.e.*, the phase diagram of the surface films (compression isotherm). A compression isotherm (see Fig. 1 *a*) has a stepwise pattern indicating changes in the character of the interaction between molecules. There are gas, liquid and solid aggregation states of thin films (see Fig. 1 *b*). Monolayers in different aggregation states are characterized by different compressibility

$$\chi = -\left[A\left(\frac{\partial \pi}{\partial A}\right)_{N,T}\right]^{-1} \quad (2)$$

(N is the number of molecules in the layer).

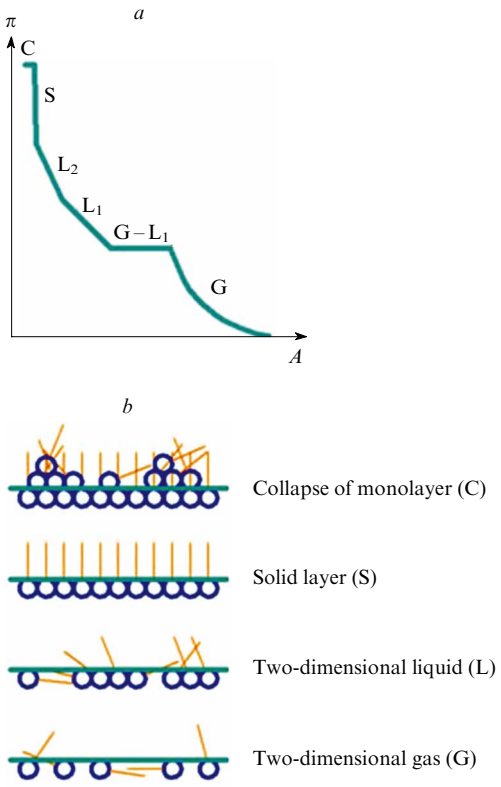


Figure 1. Compression isotherm constructed upon compression of a surfactant monolayer (*a*) and interactions between surfactant molecules in a monolayer in different aggregation states and in the case of collapse (*b*).
The capital letters denote different aggregation states of the monolayer.

The states of a film and phase transitions between them are governed by the structure of the surfactant molecule, by the interactions between polar and nonpolar fragments of the surfactant molecule, by the molecular mass, hydrophilic-lipophilic balance, as well as by the nature, temperature and pH value of the subphase.[1–7]

When a monolayer is compressed, the surface pressure can be treated as the derivative of the Gibbs free energy (G) with respect to the surface area at constant number of molecules in the layer being compressed and constant temperature[8,9]

$$\pi = -\left(\frac{\partial G}{\partial A_f}\right)_{N,T} = -\left(\frac{\partial H}{\partial A_f}\right)_{N,T} + T\left(\frac{\partial S}{\partial A_f}\right)_{N,T} \quad (3)$$

Since in a narrow temperature range the partial derivatives are temperature independent, the change in entropy upon compression of a monolayer (S_p) is

$$S_p = \left(\frac{\partial S}{\partial A_f}\right)_{N,T} \approx \left(\frac{\partial \pi}{\partial T}\right)_N \quad (4)$$

where $\partial\pi/\partial T$ is the temperature coefficient of surface pressure. If this coeficient is negative, the surface entropy of the film increases as the surface area of the film decreases.

Additional information on the state of a substance in the Langmuir monolayer can be obtained using photochemical

and rheological methods, ellipsometry, Brewster angle microscopy, fluorescence microscopy, as well as spectroscopy in various spectral regions, X-ray reflectivity, neutron reflectivity, grazing-incidence X-ray scattering, second harmonics generation, sum frequency generation and the surface potential and conductance measurements.[2]

An analysis of the behaviour of a substance in the monolayer at the air/liquid interface and the choice of the solid substrate material is followed by the preparation of LB or LS films. A monolayer prepared on the aqueous subphase is compressed by a movable barrier and kept in the compressed state at a desired surface pressure. Then, monolayers are transferred on the solid substrate in a single step or in sequence (Fig. 2).

In the case of LS transfer, the substrate is placed almost horizontally and the monolayer is then applied (see Fig. 2 *a*). The monolayer holds on the substrate by adhesive forces. If the substrate is positioned perpendicular to the layer surface, one deals with the LB transfer. When the substrate moves from the gas phase to the liquid phase, hydrophobic transfer of matter occurs (see Fig. 2 *b*); otherwise, transfer is hydrophilic (see Fig. 2 *c*). Transfer is performed with a dipper, a device which slowly draws the solid substrate up and down. To form a regular structure, the monolayer should be compressed but not too strongly because this may induce collapse of the monolayer near the defect. As monolayers are successively deposited onto the substrate, the amount of the substance on the water surface decreases and the movable barrier automatically compresses the film, thus ensuring a constant π value in the course of transfer.[3,4]

The degree of transfer of a monolayer using the LB technique is characterized by the transfer ratio (K), *i.e.*, the ratio of the decrease in the surface area of the monolayer on the water subphase (Δs_1) to the surface area of the substrate (Δs_2) covered with the transferred monolayer.

$$K = \frac{\Delta s_1}{\Delta s_2} \qquad (5)$$

Positive transfer ratio values indicate deposition of the substance on the substrate, while negative values correspond to the reverse transfer of matter from the previously covered substrate. Quantitative transfer of matter occurs at transfer ratio values of nearly unity. Multistep transfer (see Fig. 2 *d*) is carried out using a conventional procedure, *viz.*, the substrate is kept for some time in air to evaporate water, while under a water layer the substrate is stopped to relax the surface layer.[1–5]

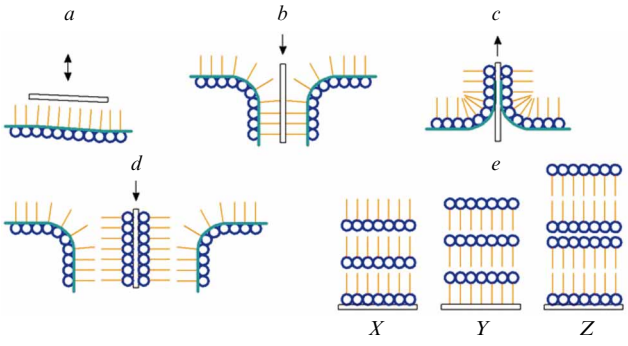


Figure 2. Different types of monolayer transfer onto solid substrates: LS transfer (*a*); LB transfer: hydrophobic (*b*) and hydrophilic (*c*); multistep transfer (*d*) and types of layered structures (*e*).

Depending on the direction of substrate motion through the monolayer, there are three types of layers (see Fig. 2 *e*), namely, two polar (types X and Z) and one symmetrical nonpolar (type Y). Successive LS transfer can give type-X or type-Z films. Multicomponent LB and LS films which, in particular, simulate biomembranes, can be prepared by, *e.g.*, transfer of mixed monolayers, successive deposition of different monolayers,[1–5] as well as by using polyion complex technique.[10]

However, the LB and LS techniques have a number of limitations, being mainly used in laboratory practice to prepare small series of samples. Changes in the hydrophilic–lipophilic balance preclude the choice of the subphase, conditions for the formation of thermodynamically stable monolayers and transfer parameters. Also, the choice of a highly volatile solvent characterized by poor miscibility with the subphase also may appear to be difficult, especially for high-molecular-mass compounds. Poor adhesion of the monolayer to the substrate leads to slow transfer. The structures of the films transferred on the solid substrates often differ from the structure of corresponding Langmuir monolayers owing to molecular reorganization under the action of variable external factors. In the case of wetting of the solid substrate upon transfer from the air/liquid interface, a very thin subphase layer is formed; this violates the dense molecular packing owing to displacement and sliding of different domains of the monolayer film relative to one another upon deposition of the monolayer and drying of LB or LS films.

II.2. Methods of investigation

II.2.a. Monolayer films

The Langmuir–Blodgett films are highly organized systems that were for the first time studied by modern structural methods, in particular, direct visualization methods originating from the invention of a scanning tunnelling microscope in 1982.[11] Initially, the scanning tunnelling microscope was designed to visualize conductive surfaces in ultrahigh vacuum on the atomic level; however, it was found that the main principles of scanning tunneling microscopy (STM) can be used to study other types of surfaces upon elaboration of a family of scanning microscopes. It was found that these instruments can not only reconstruct the surface topology of materials under study, but are also suitable for the determination of various physical properties including adhesion, local friction, elastic modulus, electric and magnetic fields, as well as specific molecular interactions. Rapid progress in the studies of the surface properties of materials is due to the invention of an atomic force microscope in 1986[12] in order to investigate insulators and semiconductors in different atmospheres. To date, various methods based on atomic force microscopy (AFM) are available.[13–15]

In spite of a variety of problems and exploration targets, which influence the design of particular types of instruments, all types of scanning microscopes include two characteristic details, namely

— an ultrathin probe which locally interacts with the surface of the material with variable force; and

— a movable piezoelectric actuator for controlling the probe position relative to the surface under study to a subnanometre accuracy.

Ultrahigh resolution of scanning tunnelling and atomic force microscopes offers great prospects for studies of composite materials and mesoporous structures. At the same time, STM and AFM have some important limitations. First of all, this is two-dimensional character of scanning procedure. In contrast to X-ray imaging and laminography, this makes it possible to study the top layers of materials (*e.g.*, fibres in the near-surface layer of a composite material under conditions that can be different from the conditions for most fibres in the matrix). Besides, the finite size of the probe (cantilever) is of great importance. Eventually, the STM or AFM image of the surface represents the convolution of the shape of the cantilever and the topography of the surface studied; pores and fibres smaller than the diameter of the cantilever are not detected by the instrument. Generally, topographic features projected above the surface (in particular, fibres on the surface of a material under study) look larger, while pits, pores, cracks, *etc*. look much smaller than their actual size.

Finally, the surface scanning procedure implies that the cantilever contacts the surface. Therefore, rather soft materials (*e.g.*, a polymer matrix) can be damaged in the course of experiments, some fragments can be displaced from their positions; this may be followed by the appearance of artifacts in the images. Taking into account this fact, the main line of development of AFM in the studies of composite polymeric materials involves elaboration of non-contact methods where the cantilever oscillating at a particular frequency is some distance off the surface. The measured response consists in modulation of these oscillations depending on the surface properties and topography. Also, the frequency shift necessary to maintain a particular mode of cantilever oscillations serves a feedback for controlling the system.[16] If an atomic force microscope operates in the dynamic tapping mode, the cantilever oscillating at a particular frequency contacts the sample surface. As a result, the amplitude of its vibrations decreases compared to the amplitude of natural oscillations. Since the cantilever contacts the surface for only a limited period of time, mechanical damage of the surface in the course of measurements is minimized, which enables investigations of various relatively soft materials, *e.g.*, polymers and biomolecules.[17,18]

The geometric parameters of the cantilever (length, thickness, shape) determine its eigenfrequency and, therefore, the potential of the atomic force microscope.[19] In particular, cantilevers with low spring constants (in this case, small forces induce a large, readily detectable displacement) and high-resonance frequencies (this avoids the development of oscillatory instabilities) are convenient for operation of microscopes in the contact mode. To achieve these properties, the cantilever should be as thin and short as possible.

The potentials of STM and AFM in visualization of surface defects on the atomic level are different.[19,20] A scanning tunnelling microscope is appropriate for reliable detection of point defects on the surface of materials because only a few atoms on the probe surface determine the tunnelling current. The AFM images of the same samples exhibit atomically smooth surfaces[19–21] owing to

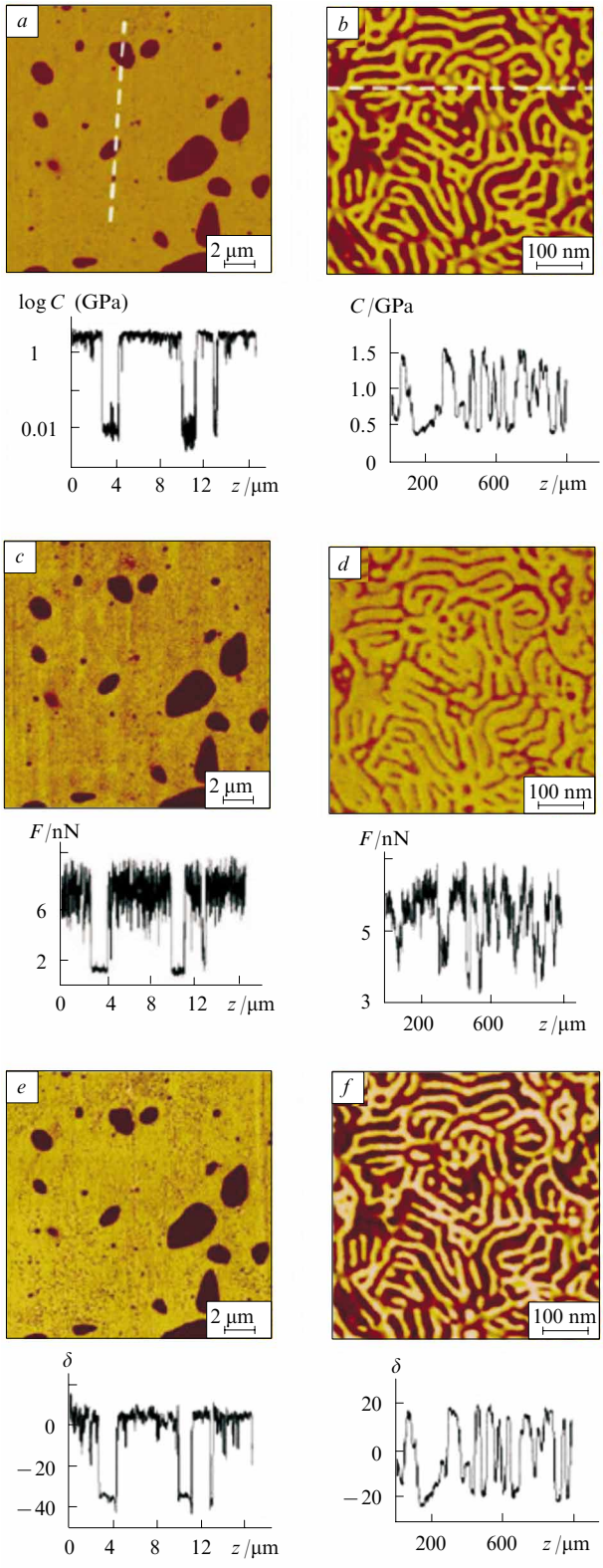


Figure 3. Nanomechanical maps obtained for thermoplastic vulcanizate (*a*, *c*, *e*) and poly(methyl methacrylate)–polyisobutylene–pole(methyl methacrylate) block copolymer (*b*, *d*, *f*) by PFT AFM.[22]
(*a*, *b*) Local elastic modulus (*C*); (*c*, *d*) peak adhesive force (*F*) (*b*, *d*, *f*); (*e*, *f*) conventional phase images, and δ is AFM scan phase. Here and in Fig. 4 *z* is the coordinate along the scan axis.

multiatomic nature of the contact between the surface of the material under study and the probe.

Atomic force microscopy in the contact mode makes it possible to achieve a high phase contrast in the studies of materials made of components with different mechanical properties. Using tailor-made probes with controlled torsion vibrations (*e.g.*, Harmonix™),[22] one can generate maps of adhesive properties and local elastic moduli of materials in the range from a few MPa to several GPa including both the matrix and main types of reinforcing fibres. The new method is called peak-force tapping atomic force microscopy (PFT AFM).

In the PFT AFM mode, the cantilever oscillates at a frequency of about 2 kHz (this is much lower than the resonance frequency of the cantilever) with an amplitude of 300 nm. This means that the probe contacts the surface over a period of a few microseconds. Owing to high data processing rate the instrument can determine the temporal dependence of the contact force. A feedback circuit makes it possible to maintain a constant value of the maximum normal component of the contact force, which enables simultaneous calculations of various mechanical properties of the surface, namely, adhesion, surface deformation, surface topography (Figs 3 and 4).

However, it should be noted that these methods are inappropriate for determining the structure of thin-film samples and its changes in the course of processing and operation; therefore, methods of investigations using X-rays, *viz.*, X-ray reflectivity and grazing-incidence X-ray diffraction, become of particular importance. Now we will briefly outline the general principles of these methods.

The propagation of a plane electromagnetic wave characterized by the electric field intensity vector

$$\mathbf{E}(\mathbf{r}) = \mathbf{E}_0 \exp(\mathrm{i}\mathbf{k}\mathbf{r})$$

through a medium with the refractive index $n(\mathbf{r})$ is described by the Helmholtz equation

$$\Delta\mathbf{E}(\mathbf{r}) + k^2 n^2(\mathbf{r})\mathbf{E}(\mathbf{r}) = 0 \qquad (6)$$

where $k = 2\pi/\lambda$ is the modulus of the wave vector $\mathbf{k}$ and λ is the wavelentgh of X-ray radiation. Let the medium contain N atoms in a unit volume, each atom being a harmonic oscillator with the resonance frequency ω_j. Then, the general equation for the refractive index of the medium has the form

$$n^2(\mathbf{r}) = 1 + N\frac{\mathrm{e}^2}{\varepsilon_0 \mathrm{m_e}} \sum_{j=1}^{N} \frac{f_j}{\omega_j^2 - \omega^2 - 2\mathrm{i}\omega\eta_j} \qquad (7)$$

Here e and $\mathrm{m_e}$ are the charge and mass of electron, respectively; the classical electron radius is given by

$$\mathrm{r_e} = \frac{\mathrm{e}^2}{4\pi\varepsilon_0 mc^2} = 2.814 \times 10^{-5}\ \text{Å}$$

f_j are the amplitudes of forced vibrations of electrons in particular atoms

$$f_j = f_j^0 + f_j'(E) + f_j''(E) \qquad (8)$$

$f_j'(E)$ and $f_j''(E)$ are respectively the dispersion and absorption corrections which depend on the radiation energy E; ω is the frequency of incident electromagnetic wave; and η_j are the damping constants. For the X-ray spectral region, one has $\omega > \omega_j$ and

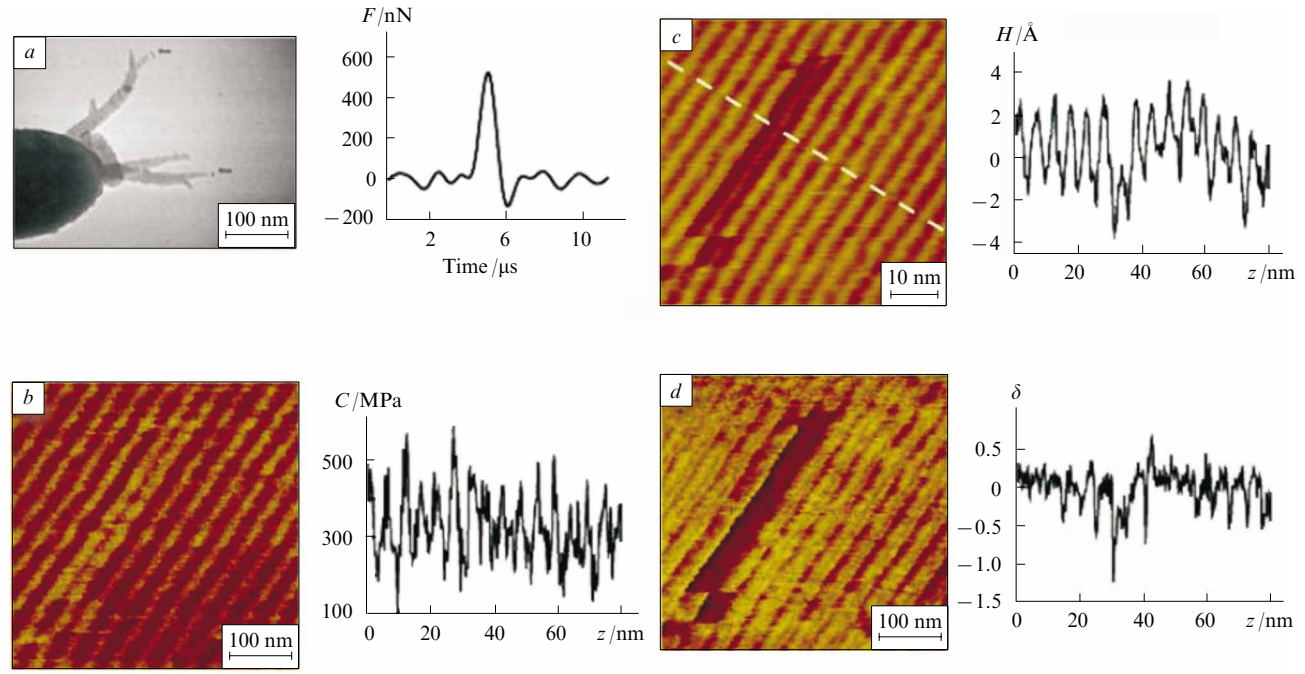


Figure 4. Nanomechanical maps obtained for samples of a long-chain alkane $C_{36}H_{74}$ by PFT AFM.[22]
(*a*) AFM image and temporal dependence of the adhesive force; (*b*) elastic modulus; (*c*, *d*) phase images; *H* is the height of the cantilever relative to the base line.

$$n(\mathbf{r}) = 1-\delta(\mathbf{r}) + \mathrm{i}\beta(\mathbf{r}) \tag{9}$$

If a medium contains Z electrons and is characterized by the electron density distribution $\rho(\mathbf{r})$, then the dispersion and absorption terms in expression (9) can be written as follows:

$$\delta(\mathbf{r}) = \frac{\lambda^2}{2\pi}\mathrm{r_e}\rho(\mathbf{r})\sum_{j=1}^{N}\frac{f_j^0 + f_j'(E)}{Z} \tag{10}$$

$$\beta(\mathbf{r}) = \frac{\lambda^2}{2\pi}\mathrm{r_e}\rho(\mathbf{r})\sum_{j=1}^{N}\frac{f_j''(E)}{Z} = \frac{\lambda}{4\pi}\mu(\mathbf{r}) \tag{11}$$

(μ is the linear absorption factor). Under grazing incidence conditions, where the wave vectors of the incident and reflected waves are close, one can admit that the functions f_j^0 are independent of $\mathbf{k}$. Then one gets

$$f_j^0 \approx Z_j$$

Thus, for a homogeneous medium with low resonance absorption the expression for the refractive index is essentially simplified

$$n = 1 - \frac{\lambda^2}{2\pi}\mathrm{r_e}\rho + \mathrm{i}\frac{\lambda}{4\pi}\mu \tag{12}$$

Since

$$\delta = \frac{\lambda^2}{2\pi}\mathrm{r_e}\rho \approx 10^{-6} > 0$$

the refractive index of X-rays is slightly lower than unity; therefore, the incidence of an X-ray beam from vacuum or air onto the surface of the condensed phase is accompanied by total internal reflection. The critical angle can be determined with ease using Snell's law assuming that the angle of refraction is equal to zero and $n = 1-\delta$

$$\alpha_{\mathrm{cr}} \approx \sqrt{2\delta} = \lambda\sqrt{\frac{\rho\mathrm{r_e}}{\pi}} \tag{13}$$

Consider the dependence of the fraction of reflected and refracted radiation on the angle of incidence of X-ray beam. Let an ideally smooth reflecting surface be in the $x0y$ plane and the $0z$ axis be normal to this plane. Let a plane electromagnetic wave $\mathbf{E}(\mathbf{r})$ with the electric field intensity vector oscillating along the $0y$ axis be incident at the grazing angle α_i. Then, one has

$$\mathbf{E}(\mathbf{r}) = (0,A,0)\exp(\mathrm{i}\mathbf{k}_i\mathbf{r})$$

where

$$\mathbf{k}_i(\mathbf{r}) = k(\cos\alpha_i, 0, -\sin\alpha_i)$$

In this case, the reflected wave $\mathbf{E}_g(\mathbf{r})$ and refracted wave $\mathbf{E}_t(\mathbf{r})$ can be described as follows:

$$\mathbf{E}_g(\mathbf{r}) = (0,B,0)\exp(\mathrm{i}\mathbf{k}_g\mathbf{r}),\ \mathbf{k}_g(\mathbf{r}) = k(\cos\alpha_i, 0, \sin\alpha_i) \tag{14}$$

$$\mathbf{E}_t(\mathbf{r}) = (0,C,0)\exp(\mathrm{i}\mathbf{k}_t\mathbf{r}),\ \mathbf{k}_t(\mathbf{r}) = k(k_{tx}, 0, k_{tz})$$

The coefficients k_{tx} and k_{tz} are related to parameters of the incident wave by the law of refraction (Snell's law). Besides, one should take into account the continuity conditions for components of the electric field intensity vector on the reflection plane.

In the case of *s*-polarization (linearly polarized incident wave; the electric field intensity vector is perpendicular to the $x0z$ scattering plane, *i.e.*, is aligned with the $0y$ axis), the ratios of the amplitudes of the reflected (r_s) and refracted (t_s) waves to the amplitude of the incident wave are

$$r_s \equiv \frac{B}{A} = \frac{k_{iz} - k_{tz}}{k_{iz} + k_{kz}} \tag{15}$$

$$t_s \equiv \frac{C}{A} = \frac{2k_{iz}}{k_{iz} + k_{tz}}\,.$$

In the case of *p*-polarization (linearly polarized incident wave; the electric field intensity vector oscillates in the $x0z$ scattering plane) one has

$$r_p \equiv \frac{B}{A} = \frac{n^2k_{iz} - k_{tz}}{n^2k_{iz} + k_{tz}} \tag{16}$$

$$t_p \equiv \frac{C}{A} = \frac{2k_{iz}}{n^2k_{iz} + k_{tz}}$$

Since the refractive index of any surface is close to unity, differences between the two cases can be neglected. Also, taking into account the fact that the angles in the grazing incidence conditions are small and the Fresnel reflectance of X-ray radiation is

$$R_{\mathrm{F}} = |r|^2$$

one gets

$$R_{\mathrm{F}} = \frac{(\alpha_i - p_+)^2 + p_-^2}{(\alpha_i + p_+)^2 + p_-^2} \tag{17}$$

where p_+ and p_- are respectively the real and imaginary parts of the complex angle of refraction

$$p_\pm^2 = \frac{\sqrt{(\alpha_i^2 - \alpha_{\mathrm{cr}}^2)^2 + 4\beta^2} \pm (\alpha_i^2 - \alpha_{\mathrm{cr}}^2)}{2} \tag{18}$$

Analogously, the intensity of the refracted beam is

$$T_{\mathrm{F}} = |t|^2 = R_{\mathrm{F}}\,\frac{4\alpha_i^2}{(\alpha_i - p_+)^2 + p_-^2} \tag{19}$$

The reflectance and transmittance of X-rays ($\lambda = 1.54$ Å) through a smooth silica surface ($\delta = 7.56\times10^{-6}$) are plotted in Fig. 5 for different values of the absorption and dispersion components of the refractive index. As can be seen, the R_{F} function abruptly decreases at $\alpha_i > \alpha_{\mathrm{cr}}$

$$R_{\mathrm{F}} \approx \left(\frac{\alpha_i}{\alpha_{\mathrm{cr}}}\right)^{-4}$$

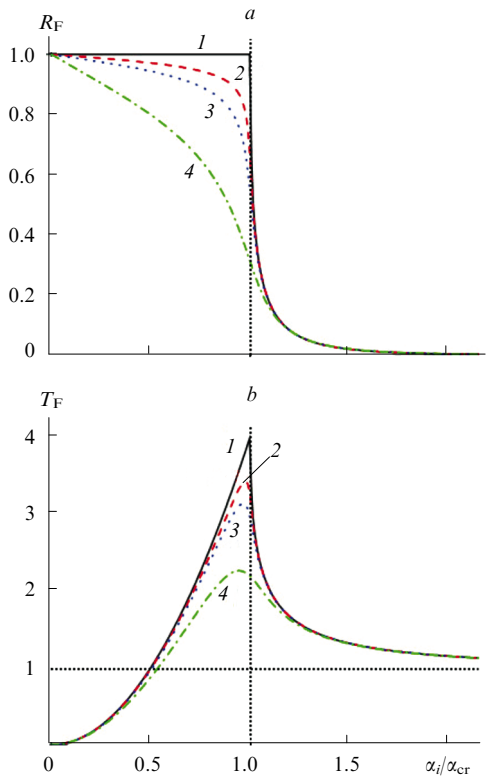


Figure 5. The reflectance and (*a*) and transmittance (*b*) of X-rays (λ = 1.54 Å) through a smooth silica surface ($\delta = 7.56 \times 10^{-6}$) at different ratios of the absorption and dispersion components of the refractive index.
β/δ = 0 (*1*), 0.025 (*2*), 0.05 (*3*), 0.2 (*4*).

This is the reason for specific features of X-ray reflectivity, related to the need for detection of the reflected beam in a very wide intensity range, namely, a change in the angle of incidence from $0.2\,\alpha_{cr}$ to $3.0\,\alpha_{cr}$ causes the surface reflectance to decrease by at least six orders of magnitude.

Besides, the penetration depth (D) of an X-ray beam into the material depends strongly on the angle of incidence near the critical angle.

$$D = \frac{\lambda}{\sqrt{2}\pi\sqrt{\sqrt{(\alpha_i^2 - \alpha_{cr}^2)^2 + 4\beta^2} - (\alpha_i^2 - \alpha_{cr}^2)}} \qquad (20)$$

Combining the reflectance and absorption functions and the penetration depth of the X-ray beam makes it possible to obtain a depth profile of a thin-film material, because at a specified angle of incidence the observed response of the material is due to reflection from a relatively thin layer located at a particular depth in the film interior.[23, 24]

II.2.b. Multilayer films. Parratt's method

An important consequence of expression (20) is the possibility of studying the depth profile of the electron density distribution. Consider a material comprised of N ideally smooth layers. Let us measure the $0z$ coordinate and enumerate layers from the top film/vacuum interface ($z_1 = 0$, $N = 1$). Let the thickness and the refractive index of the jth layer be

$$z_{j-1} - z_j \equiv d_j$$

and

$$n_j = 1 - \delta_j + i\beta_j$$

respectively.

Let $\mathbf{k}_{ij}$ be the wave vector and T_j be the amplitude of an X-ray beam passing through the jth layer. Let $\mathbf{k}_{ij}$ and R_j be the wave vector and amplitude of the beam reflected from the jth layer, respectively. Similarly to the derivation of Eqns (17) and (19), the continuity condition for the electric field strength vector should be met at each interface. Parratt[25] elaborated a recursive procedure for solving the system of equations and thus obtained

$$X_j \equiv \frac{R_j}{T_j} = \exp(-2ik_{zj}z_j)\,\frac{r_{j,j+1} + X_{j+1}\exp(2ik_{z\,j+1}z_j)}{1 + r_{j,j+1}X_{j+1}\exp(2ik_{z\,j+1}z_j)} \qquad (21)$$

where the amplitude of the beam reflected from the jth surface is determined by expression (15) and Snell's law. Prior to starting the recursive procedure, assume that the film is sufficiently thick and there is no reflection from the substrate, $R_{N+1} = 0$. Then one has

$$R_{j+1} = \frac{T_j r_{j+1,j}\exp[-i(k_{z\,j+1} + k_{zj})z_j] + R_j\exp[-i(k_{z\,j+1} - k_{zj})z_j]}{t_{j+1,j}}$$
$$T_{j+1} = \frac{T_j\exp[-i(k_{z\,j+1} - k_{zj})z_j] + R_j r_{j+1,j}\exp[i(k_{z\,j+1} + k_{zj})z_j]}{t_{j+1,j}} \qquad (22)$$

The characteristic reflectivity curve (Fig. 6) is a descending curve described by a fourth-order equation with superimposed periodic interference pattern (so-called Kiessig fringes[26] originating from the interference of X-rays reflected from the air/material and material/substrate interfaces). The width of the Kiessig fringes is immediately related to the film thickness (d), one of the most important parameters determined using X-ray reflectivity

$$d = \frac{2\pi}{\Delta q_z} \qquad (23)$$

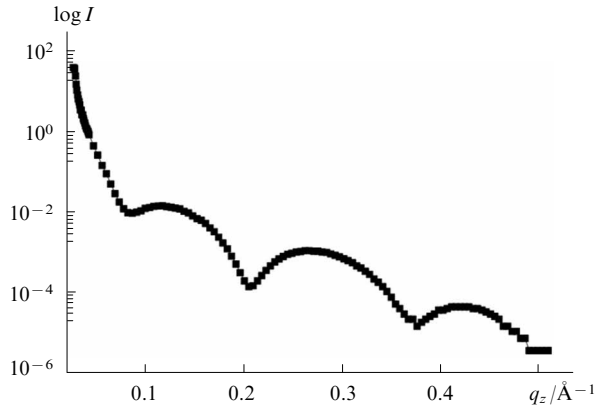


Figure 6. A characteristic X-ray reflectivity curve obtained for thin films of a hemocyanin dye on a smooth surface of silica (substrate).

where Δq_z is the distance between two neighbouring minima in the reflectivity curve.

II.2.c. Rough surfaces

In an ideal case of smooth interfaces the refractive index of a film depends only on its height (z) above the substrate surface. All real surfaces are rough; therefore, in the general case the refractive index should be considered as function of three coordinates

$$n = n(x, y, z).$$

Since X-ray reflectivity implies investigations of a mirror reflected beam, one has

$$\mathbf{q} = \mathbf{k} - \mathbf{k}_i = \mathbf{q}(z)$$

and, correspondingly, the observed response of the system makes it possible to determine the surface structure averaged over the (x, y) plane

$$n_j(z) = \int\int n_j(x, y, z)\mathrm{d}y\mathrm{d}x \tag{24}$$

Thus, a rough surface can be represented by a set of ideally smooth surfaces arranged at the distance z from the interface. If these local surfaces are described by the probability density $P_j(z)$ with an average value

$$\mu_j = \int zP_j(z)\mathrm{d}z \tag{25}$$

and the root-mean-square roughness

$$\sigma_j^2 = \int(z - \mu_j)^2 P_j(z)\mathrm{d}z, \tag{26}$$

the Fourier transformation of the functions $P_j(z)$ gives

$$f_j(k) = \exp(\mathrm{i}k\mu_j)\int \exp(-\mathrm{i}kz)P_j(z)\mathrm{d}z$$

Having averaged Eqns (17) and (19), one gets

$$R_{j+1} = \frac{T_j\tilde{r}_{j+1,j}\exp[-\mathrm{i}(k_{zj+1} + k_{zj})z_j] + R_j\exp[-\mathrm{i}(k_{zj+1} - k_{zj})z_j]}{\tilde{t}_{j+1,j}} \tag{27}$$

$$T_{j+1} = \frac{T_j\exp[\mathrm{i}(k_{zj+1} - k_{zj})z_j] + R_jf_r\tilde{r}_{j+1,j}\exp[\mathrm{i}(k_{zj+1} + k_{zj})z_j]}{f_t\tilde{t}_{j+1,j}}$$

where the corresponding Fresnel coefficients $\tilde{r}_{j+1,j}$ and $\tilde{t}_{j+1,j}$ are given by

$$\tilde{r}_{j+1,j} = \frac{f_j(k_{zj+1} + k_{zj})}{f_j(k_{zj+1} - k_{zj})}\, r_{j+1,j} \tag{28}$$

$$\tilde{t}_{j+1,j} = \frac{1}{f_j(k_{zj+1} - k_{zj})}\, t_{j+1,j}$$

and the functions f_r and f_t are defined as follows:

$$f_r = \frac{f_j(k_{zj+1} - k_{zj})}{f_j(-k_{zj+1} + k_{zj})}\,\frac{f_j(-k_{zj+1} - k_{zj})}{f_j(k_{zj+1} + k_{zj})} \tag{29}$$

$$f_t = \frac{f_j(k_{zj+1} - k_{zj})}{f_j(-k_{zj+1} + k_{zj})}.$$

Theoretical studies of X-ray reflection from a film of complex composition require an additional assumption of the material (and, correspondingly, the refractive index) distribution between the jth and $(j+1)$th layers. One can admit that

$$n_j(z) = \frac{n_j + n_{j+1}}{2} - \frac{n_j - n_{j+1}}{2}\,\mathrm{erf}\left(\frac{z - z_j}{\sqrt{2}\sigma_j}\right) \tag{30}$$

where

$$\mathrm{erf}(z) = \frac{2}{\sqrt{\pi}}\int_0^z \exp(-t^2)\mathrm{d}t \tag{31}$$

(here t is the integration variable), and a Gaussian probability density distribution

$$P_j(z) = \frac{1}{\sqrt{2\pi}\sigma_j}\exp\left(-\frac{z^2}{2\sigma^2}\right) \tag{32}$$

As a result, one has

$$\tilde{r}_{j+1,j} = r_{j+1,j}\exp(-2k_{zj}k_{zj+1}\sigma_j^2) \tag{33}$$

$$\tilde{t}_{j+1,j} = t_{j+1,j}\exp\left[-\frac{(k_{zj} - k_{zj+1})^2\sigma_j^2}{2}\right]$$

Using the mean field theory, it was shown[27] that the liquid phase distribution at the liquid/vapour interface has the hyperbolic tangent profile

$$n_j(z) = \frac{n_j + n_{j+1}}{2} - \frac{n_j - n_{j+1}}{2}\,\tanh\left(\frac{\pi}{2\sqrt{3}}\,\frac{z - z_j}{\sigma_j}\right) \tag{34}$$

with the probability density given by

$$P_j(z) = \frac{\pi}{4\sqrt{3}\sigma_j}\cosh^{-2}\left(\frac{\pi}{2\sqrt{3}}\,\frac{z}{\sigma_j}\right) \tag{35}$$

In this case, the modified Fresnel coefficients are

$$\tilde{r}_{j+1,j} = r_{j+1,j}\,\frac{\sinh[\sqrt{3}\sigma_j(k_{zj} - k_{zj+1})]}{\sinh[\sqrt{3}\sigma_j(k_{zj} + k_{zj+1})]} \tag{36}$$

$$\tilde{t}_{j+1,j} = t_{j+1,j}\,\frac{\sinh[\sqrt{3}\sigma_j(k_{zj} - k_{zj+1})]}{\sqrt{3}\sigma_j(k_{zj} - k_{zj+1})}$$

This result also holds for the interface between two mutually insoluble polymers.[28–32] It should be noted that the intensity differences calculated for the reflected and refracted beams from Eqns (33) and (36) are at most 5% at the experimentally admissible angles of incidence (up to $\alpha_i = 5\alpha_{cr}$). Besides, $|\tilde{r}_{j+1,j}| < |r_{j+1,j}|$, *i.e.*, the surface roughness always leads to a decrease in the intensity of the reflected X-ray beam. The experimentally observed decrease in intensity is even more pronounced due to the shading

effect, namely, scattering of the beam reflected from a pit on the surface by protrusions.

II.2.d. Electron density reconstruction methods

In the aforesaid, we described methods for modelling the intensity of scattering from almost any surface. Now we will consider the possibility to solve the inverse problem, *i.e.*, to reconstruct the thin film structure from the shape of the reflectivity curve. Let $\rho(x, y, z)$ be the electron density function characterizing the distribution of scattering elements in the film. In the first Born approximation (possible secondary scattering is ignored), one can show [33–35] that the intensity of reflected beam is proportional to the Fourier transform of the electron density derivative with respect to the film thickness

$$R(q_z) = R_F(q_z)\left|\frac{1}{\rho_\infty}\int\frac{d\rho(z)}{dz}\exp(iq_z z)dz\right|^2 = R_F(q_z)|F(q_z)|^2 \quad (37)$$

where ρ_∞ is the average electron density of the sample, $\rho(z)$ is the electron density averaged in the plane perpendicular to the film surface, $R_F(q_z)$ is the Fresnel reflectance (17) and $F(q_z)$ is the scattering form factor.

Thus, one has

$$\rho'(z) = \int F(q_z)\exp(iq_z z)dq_z \quad (38)$$

$$F(q_z) = |F(q_z)|\exp[i\varphi(q_z)] \quad (39)$$

Next, we assume that the electron density profile can be 'guesses' using additional data, *e.g.*, results of molecular modelling. An important additional assumption (trivial case for all real physical systems) consists in that the electron density function is non-negative at any point. Also, the film thickness can be calculated from the width of the Kiessig fringes using Eqn (23). Let us write Eqns (38) and (39) for the 'guesses' solution $\rho_m(z)$ (see Refs 36–38)

$$\rho'_m = \int F_m(q_z)\exp(iq_z z)dq_z \quad (40)$$

$$F_m(q_z) = |F_m(q_z)|\exp[i\varphi_m(q_z)] \quad (41)$$

Generally, the 'guesses' phase $\varphi_m(q_z)$ can differ from the real (unknown) phase $\varphi(q_z)$; therefore, one has

$$\varphi(q_z) = \varphi_m(q_z) + \Delta\varphi(q_z) \quad (42)$$

Combining Eqns (38)–(42), one gets

$$\rho'(z) = \int\int\sqrt{\frac{R(q_z)}{R_m(q_z)}}\exp[i\Delta\varphi(q_z)]\rho'_m(z_1)\exp[iq_z(z-z_1)]dz_1 dq_z \quad (43)$$

Note that Eqn (43) is an exact analytical expression. To simplify it in order to derive an analytical form of the function $\rho'(z)$, one can, *e.g.*, assume that

$$\Delta\varphi(q_z) \cong 0$$

In some cases, this approximation gives realistic results.[36]

Consider a more exact solution using the notion of Hilbert phases.[39] According to the Titchmarsch theorem, if a $f(z)$ is zero on a domain, *e.g.*, $f(z) = 0$ for $z < 0$, then its Fourier transform $g(q)$ is an analytical function in the upper half of complex q plane. From the Cauchy principal value theorem it follows that Re $g(q)$ and Img $g(q)$ are Hilbert transforms. An example of application of the Titchmarsch theorem in solid state physics is provided by the Kramers–Kronig relations, which determine the real and imaginary parts of the refractive index.

In X-ray reflectivity, a thin film is always placed on a substrate with almost constant electron density. If the $0z$ axis is directed upward (towards the thin film) and the z coordinate is measured from the substrate surface, the electron density derivative $\rho'(z)$ will be zero for $z < 0$. Then, from the Titchmarsch theorem it follows that the scattering form factor is an analytical function in the upper half of complex q plane and its real and imaginary parts are two Hilbert transforms equivalent to the dispersion relations. Besides, $\ln F(q_z)$ is also an analytic function except the points q_z where the scattering form factor becomes equal to zero. If $F(q_z) \neq 0$ for all q_z and $\mathrm{Im}(q_z) > 0$, then the Hilbert phase

$$\varphi_H(q_z) = -\frac{2q_z}{\pi}\int_0^\infty\frac{\ln\left[|F(q'_z)|/|F(q_z)|\right]}{(q'_z)^2 - q_z^2}dq'_z \quad (44)$$

and the real phase of the scattering form factor

$$\varphi(q_z) = \arctan\left\{\frac{\mathrm{Im}[F(q_z)]}{\mathrm{Re}[F(q_z)]}\right\} \quad (45)$$

coincide.

Thus, the phase problem in reconstruction of the electron density profile is reduced to answer to the question whether or not the scattering form factor becomes equal to zero in the upper half of q plane. A simple method to avoid singularities in the integral (44) when performing numerical analysis of reflectivity curves is available.[40] A practically important class of electron density profiles for which the condition $F(q_x) \neq 0$ is always met includes stacks comprising N layers of constant electron density. In this case one has

$$\rho(z)' = \sum_{m=1}^{N}\Delta\rho_m\delta(z - z_m) \quad (46)$$

where z_m are the heights of layer borders. Electron density reconstruction from the reflectivity curves obtained for such samples makes it possible to obtain an analytical solution to Eqn (43) provided that

$$|\Delta\rho_1| > \sum_{m=2}^{N}|\Delta\rho_m|$$

Summing up, generally, it is more appropriate to use the Hilbert phase $\varphi_{H,m}(q_z)$ as the 'guesses' phase $\varphi_m(q_z)$. The general algorithm of reconstructing the electron density profile of thin films from the reflectivity curves using the 'guesses' phase method involves the following steps:[38]

— measurements of experimental reflectivity curves $R(q_z)$ from samples with the electron density profile $\rho(z)$ and determination of the experimental error;

— simulation of the 'guesses' profile $\rho_m(z)$ using *a priori* information on the layer structure;

— calculations of the reflectivity curve $R_m(q_z)$ from the 'guesses' profile using Eqn (37) or Parratt's formalism;

— determination of the difference between the Hilbert phases

$$\Delta\varphi(q_z) = \varphi_{\mathrm{H}}(q_z) - \varphi_{\mathrm{H},m}(q_z) \tag{47}$$

where

$$\Delta\varphi(q_z) = \frac{q_z}{\pi}\int_0^{\infty} \frac{\ln\left\{\left[R_m(q'_z)R(q_z)\right]/\left[R_m(q_z)R(q'_z)\right]\right\}}{(q'_z)^2 - q_z^2}\,\mathrm{d}q'_z \tag{48}$$

— calculations of the electron density profile $\rho_{m+1}(z)$ using Eqn (43)

$$\rho_{m+1}(z) = \int_{-\infty}^{z}\int_{-\infty}^{+\infty}\int_{-\infty}^{+\infty}\sqrt{\frac{R(q_z)}{R_m(q_z)}}\exp\left[\mathrm{i}\Delta\varphi(q_z)\right] \times \tag{49}$$

$$\times\ \rho'_m(z_1)\exp\left[\mathrm{i}q_z(z-z_1)\right]\mathrm{d}q_z\mathrm{d}z_1\mathrm{d}z_2$$

— determination of the new reflectivity curve $R_{m+1}(q_z)$ from the calculated electron density profile $\rho_{m+1}(z)$;

— if the difference between the calculated reflectivity curve $R_{m+1}(q_z)$ and the experimental dependence $R(q_z)$ is less than the measuring error, then $\rho_{m+1}(z) = \rho(z)$; otherwise, $\rho_{m+1}(z)$ is taken as the new 'guessed' electron density profile and the difference between the Hilbert phases is calculated again (see above).

II.2.e. X-Ray experimental design. Grazing-incidence X-ray diffraction

A general design of grazing-incidence X-ray diffraction experiments is presented in Fig. 7. Let an electromagnetic wave with the wave vector $\mathbf{k}_{\mathrm{in}}$ be incident on a reflecting surface at a small angle α; as a result, a reflected wave with the wave vector $\mathbf{k}_{\mathrm{out}}$ emerges.

Let us rotate the sample plane about a normal to it. Then, at a particular arrangement of the film the wave can make a Bragg angle (Θ_d) with an atomic plane in the monolayer (with a period of d), which is oriented perpendicular to the monolayer surface. The propagation direction of the resultant diffracted wave makes the angle β with the sample plane.

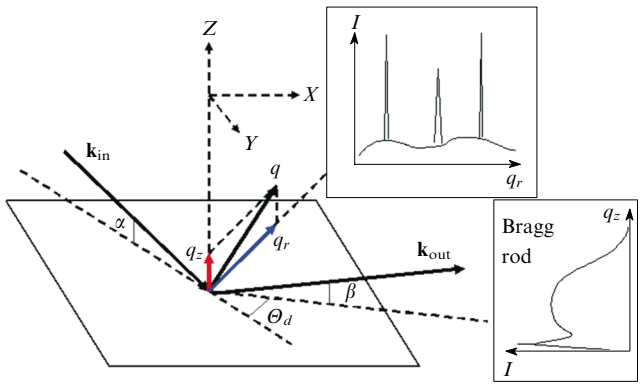


Figure 7. Grazing-incidence X-ray diffraction: an experimental design.

It should be noted that grazing-incidence X-ray diffraction is a particular case of Laue diffraction. Namely, if a sample set in Laue geometry conditions is rotated by 90° about the reciprocal lattice vector, the Bragg angle remains unchanged and the crystal setting corresponds to grazing-incidence X-ray diffraction conditions. Similarly to Laue diffraction, grazing-incidence X-ray diffraction is characterized by the presence of Borrmann and anti-Borrmann wave fields with weaker and stronger interaction with the crystal lattice, respectively. Two-dimensional diffraction patterns bear key information on the molecular packing in the surface layers.

II.2.f. The method of X-ray standing waves

The method of X-ray standing waves,[41,42] which enables determination of atomic coordinates in the crystal lattice, occupies a particular place in the studies of subtle details of the surface structure, surface defects and impurity sublattices. It is based on the use of spatially modulated electromagnetic field appearing in the crystal in the case of dynamical diffraction, in order to excite a secondary radiation (in particular, fluorescence X-ray radiation or photoelectron radiation) of atoms constituting the crystal. A standing wave with a period equal to the lattice constant, 'senses' minor deviations of atomic planes (or particular atoms) from their exact positions in the crystal. An analysis of the angular dependence of the characteristic secondary radiation within the dynamical diffraction region enables high-precision determination of corresponding atomic positions relative to the system of diffraction planes and characterization of disorder in the atomic subsystem.

The potential of the method of X-ray standing waves, which combines the structural (diffraction) resolution with spectroscopic sensitivity, was demonstrated taking analysis of the structures of multicomponent crystals as examples.[43–46] It should be noted that practical implementation of the method of X-ray standing waves faces severe experimental difficulties because one should ensure high-precision angular positioning of the crystal and spectroscopically sensitive detection of secondary radiation.

Let a plane electromagnetic wave with the wave vector $\mathbf{k}_0$ be incident on a crystal. Propagation of the wave in the crystal can be described by Bloch waves that take into account translational symmetry of the crystal and represent a coherent superposition of the refracted and scattered waves

$$\mathbf{k}_{\mathrm{m}} = \mathbf{k}_0 + \mathbf{h}_{\mathrm{m}}$$

where $\mathbf{h}_{\mathrm{m}}$ is the reciprocal lattice vector.

Amplitudes of the scattered waves are determined from the Maxwell equations (see above). Usually, they are very small, being much smaller than the amplitudes of refracted waves, because in the X-ray frequency region the dielectric permittiviy of the medium is close to unity. Therefore, the Bloch waves emerging in the crystal almost coincide with the incident plane wave. However, if the Bragg condition is met for a reciprocal lattice vector, the amplitude of the diffracted wave becomes comparable with the amplitude of the refracted wave (two-wave approximation). In this case, neglecting weak scattered waves, the amplitude of the electric field strength vector in the crystal is

$$\mathbf{E}(\mathbf{r}) = E_0\exp(\mathrm{i}\mathbf{k}_0\mathbf{r}) + E_h\exp(\mathrm{i}\mathbf{k}_h\mathbf{r}) \tag{50}$$

where E_0 and E_h are the amplitudes of the refracted and reflected waves, respectively;

$$\mathbf{k}_h = \mathbf{k}_0 + \mathbf{h}$$

Then, the field intensity is given by

$$I(\mathbf{r}) = |E_0|^2 \left[1 + \frac{|E_h|^2}{|E_0|^2} + 2\frac{|E_h|}{|E_0|}\cos(\mathbf{hr} + \alpha)\right] \quad (51)$$

where α is the phase of the E_h/E_0 ratio.

The structure of the standing wave (51) is governed by two parameters, *viz*., the ratio $|E_h|/|E_0|$ and the phase α. Depending on particular experimental conditions (deviation of the angle of incidence from the Bragg angle; geometry of the diffraction experiment), these parameters can take different values. For instance, consider a combination $|E_h| = |E_0|$ + variable phase α. In this case, the maximum field intensity is four times higher than the intensity of the refracted wave field while the minimum intensity is exactly zero. Mutual arrangement of atomic planes, *i.e*., maxima of the electron density distribution in the crystal, and maximum wave field intensity planes is determined by the phase α. For instance, at $\alpha = 0$, the field intensity maxima lie on the atomic planes, while at $\alpha = -\pi$, the atomic planes correspond to the wave field nodes. Clearly, the character of the interaction of the X-ray wave field with the crystal in the two limiting cases is significantly different. This situation occurs in the phase-sensitive range of the angles of incidence, corresponding to the region of total reflection of X-rays (see above).

If $|E_h| < |E_0|$, a standing wave still appears in the crystal, but its amplitude is smaller than in the preceding case. In the limit $|E_h| \to 0$ (large deviations from the Bragg angle), the amplitude of intensity oscillations of the standing wave tends to zero and the average intensity becomes equal to the intensity of the plane incident wave. In other words, one deals with transtion from the two-wave to the one-wave approximation.

The effect involving the existence of standing waves and variation of the total field at the atoms in the crystal lattice has long been known. However, in the classical X-ray diffraction experiments with separate detection of the intensities of the reflected and transmitted waves this effect is weak. This is due to the fact that the amplitude of inelastic scattering is much smaller than that of elastic scattering. Standing waves in the crystal can be detected in conventional X-ray experiments only as anomalous angular dependence of absorption (the anomalous transmission effect in the Laue geometry, as discovered by Borrmann [47,48]) and as weak asymmetry of the diffractive reflection curve in the Bragg geometry.[49–51] A straight and natural method of investigation and practical application of X-ray standing waves is detection of secondary radiation emerging upon absorption of X-ray quanta. These first of all concerns X-ray photoelectrons, Auger electrons, fluorescence quanta, thermal diffuse scattering and Compton scattering.

Consider a simple case where the surface of a perfect crystal is covered with a layer of foreign atoms. For simplicity, we will restrict ourselves to symmetric diffraction in the Bragg geometry, where the reflected wave emerges from the crystal from the same surface through which radiation has entered the crystal. In this case, the angular dependence of the field amplitude ratio $|E_h|/|E_0|$ and the phase α for radiation with normal polarization (σ-field) has the form [52–56]

$$\frac{|E_h|}{|E_0|}\,e^{i\alpha} = -\frac{y - iy_0 + \sqrt{(y - iy_0)^2 - (1 - iy_h)}}{1 - iy_h} \quad (52)$$

where

$$y = -\frac{\sin 2\theta_B}{|\chi_{rh}|}(\theta - \theta_B) \quad (53)$$

$$y_0 = \frac{\chi_{10}}{|\chi_{rh}|}$$

$$y_h = \frac{\chi_{1h}}{|\chi_{rh}|}$$

θ is the angle of incidence of X-ray radiation on the crystal; θ_B is the kinematic Bragg angle (ignoring refraction); χ_{rh}, $-\chi_{10}$ and χ_{1h} are respectively the Fourier components of the real and imaginary parts of the crystal polarizability

$$\chi = \chi_r + i\chi_1$$

The angular dependences of the wave field intensity calculated using expression (51) taking into account relationships (52) and (53), for reflection from the (220) atomic planes of a silicon crystal (CuK_α radiation) are shown in Fig. 8, which also demonstrates the angular dependences of the reflection coefficient of X-rays, the phase α and the interference absorption coefficient μ

$$\mu = \frac{2}{L_{ex}}\,\mathrm{Re}\sqrt{(y - iy_h)^2 - (1 - iy_0)^2} \quad (54)$$

where

$$L_{ex} = \frac{\lambda \sin\theta_B}{\pi|\chi_{rh}|} \quad (55)$$

is the extinction length and λ is the wavelength of X-rays.

As can be seen, the intensity of the wave field at atoms in the central portion of the reflection curve abruptly changes

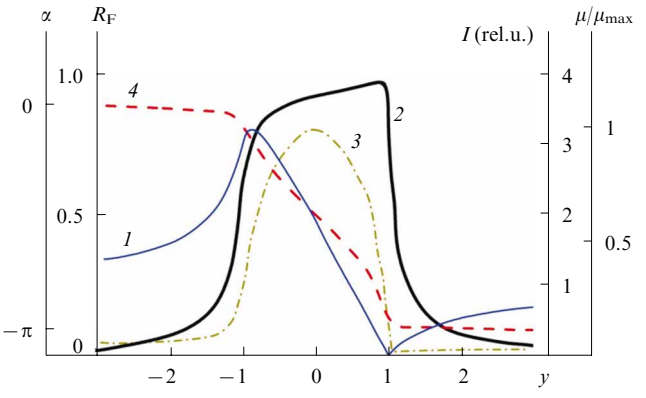


Figure 8. Angular dependences of the wave-field intensity (I) (*1*), reflection coefficient (R_F) (*2*), relative interference absorption coefficient (μ/μ_{max}) (*3*) and phase α (*4*).[41]

with the angle of incidence of X-rays on the crystal, unlike the reflection coefficient which remains almost unchanged in this range of angles. It should be noted that the phase of the complex reflection amplitude depends strongly on the angle of incidence. When measuring the intensity of the reflected beam, which is proportional to the squared modulus of the reflection amplitude, the phase information is lost. At the same time, the intensity of the wave field at the atom, which is equal to the squared modulus of the sum of the amplitudes of two coherent waves, refracted wave (E_0) and reflected wave (E_h), bears this phase. The situation is analogous to recording the phase of the scattering amplitude in holography; in our case, the role of the reference beam is played by the refracted beam. Interestingly, this opens the way to direct solution to the phase problem in structural analysis. However, one should keep in mind that the case in point is a very narrow range of angles, namely, of the order of a few angular seconds. This is due to very small scattering amplitudes of X-rays $|\chi_{rh}|$ by the unit cell of the crystal.

Thus, the intensity of the wave field at the atoms in the crystal bears a larger amount of information. Naturally, a question arises as to how to record this information using some experimental technique and then utilize it. A possible way is to detect and record the intensity of the yield of secondary radiation, *e.g.*, characteristic fluorescence from a layer of foreign atoms arranged on the surface of a single crystal, which is proportional to the local intensity of the wave field.

Consider Fig. 9 *a*. If all the foreign atoms lie strictly in the same plane and the position of the plane coincides with the correct position of the yield of reflecting planes in the crystal, the angular dependence of the yield of fluorescence from these atoms will match the angular dependence of the wave field intensity presented in Fig. 8.

The actual situation, even as applied to a monolayer of atoms adsorbed on the surface of a perfect crystal, can be much more complicated. First, this layer can have any position, which is determined by the length of the chemical bonds formed by these atoms with the atoms of the matrix crystal. Next, this layer can be partially disordered, *i.e.*, the constituent atoms can be displaced randomly from their mean positions, and the experimentally determined diffraction pattern includes contributions from all atoms in the layer. For instance, in Fig. 9 *b* the layer of our interest is displaced by half the interplanar spacing in the matrix crystal. Consequently, an additional phase $P_c = \pi$ appears in Eqn (51) in the first order of reflection. This leads to an abrupt change in the character of the angular dependence of the fluorescence yield from the impurity atoms. Indeed, whereas the maxima of the field intensity (antinodes) coincide with the positions of the atoms in the reflecting planes of the matrix crystal, the position of the layer of impurity atoms corresponds to the field minima (nodes), and *vice versa*. Therefore, the curve of the angular dependence (its phase-sensitive portion) proves to be a mirror image of the previously discussed case (see Fig. 9 *a*).

A fundamentally different situation arises when the layer of impurity atoms is highly disordered (see Fig. 9 *c*). Here, there are no preferential (coherent) atomic positions with respect to the standing wave, and nearly equal proportions of atoms lie simultaneously at the antinodes and nodes of the wave field. Clearly, the yield of fluorescence from such a layer is described by expression (51) without the third (interference) term, which vanishes after averaging over coordinates of all atoms in the layer. Here the shape of the curve of the secondary radiation yield reproduces the shape of the X-ray reflection curve but bears no phase information.

The actual pattern is intermediate between the limiting cases discussed above, *i.e.*, the atomic layer can be partially disordered and displaced. Statistical averaging of expression (51) over the coordinates of all atoms in the layer gives the following expression for the angular dependence of fluorescence:

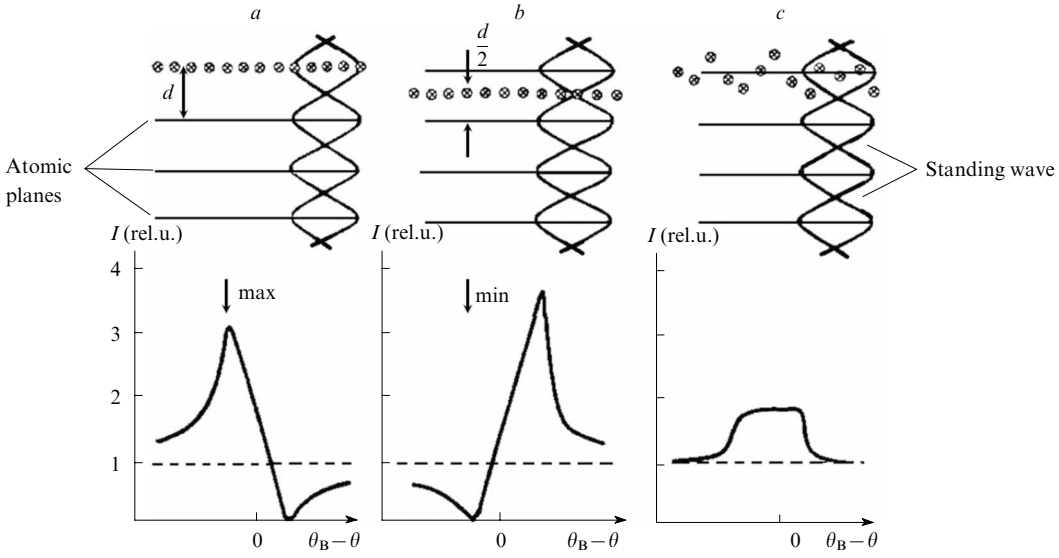


Figure 9. Diagrams illustrating different positions of impurity atoms relative to the antinodes of the wave field and the corresponding yields of secondary radiation; (*a* – *c*) see text.

$$I = I_0\left[1 + \frac{|E_h|^2}{|E_0|^2} + 2\frac{|E_h|}{|E_0|}\cos(P_c + \alpha)\right] \quad (56)$$

where

$$P_c = \mathbf{hr}_c = \frac{2\pi n z_c}{d} \quad (57)$$

parameter z_c is the coherent position (*i.e.*, the position of the mean plane of the impurity atoms with respect to the diffraction planes of the crystal); it is related to the coherent fraction F_c (Debye – Waller factor), which describes the root-mean-square statistical and thermal displacements of the atoms from the mean position

$$F_c = \langle\exp[i\mathbf{h}(\mathbf{r} - \mathbf{r}_c)]\rangle = \exp\left[-\frac{1}{2}h^2\langle(z - z_c)^2\rangle\right] \quad (58)$$

Summing up, from the aforesaid it follows that the shape of the angular dependence of the fluorescence yield allows one to directly measure the coherent position (and thus the lengths of the chemical bonds between atoms of the matrix crystal and impurity atoms) and the coherent fraction with high accuracy.

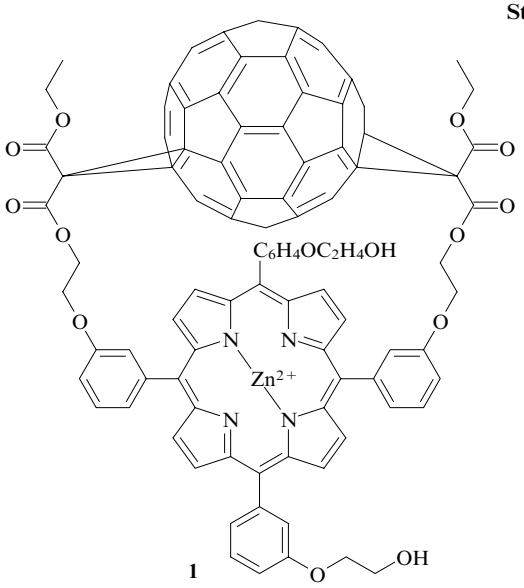
The thought experiment we have discussed was actually performed in a study[57] of fluorescence of bromine atoms chemisorbed on the surface of a Si single crystal using the (220) reflection of MoK_α radiation. Processing of experimental angular dependences of the fluorescence yield gave $F_c = 0.3$ and $z_c = 1.73 \pm 0.07$ Å. The latter value is in good agreement with the length of the Si – Br covalent bond.

Combining the methods of X-ray standing waves, X-ray reflectivity and grazing-incidence X-ray diffraction, one can perform high-precision structural studies of thin-film materials.

Consider monolayers of molecules of porphyrin – fullerene dyad **1** with Zn atom (fluorescent label) incorporated into the porphyrin ring on the surface of a liquid subphase.[58]

Molecular modelling of this structure revealed three fragments differing in electron density, *viz.*, a fullerene-containing layer, an intermediate layer and a porphyrin-containing layer. In compound **1**, hydrophilic groups are attached to the porphyrin ring; therefore, molecules on the liquid surface should be oriented in such a manner that the porphyrin ring faces water.

Structure 1



1

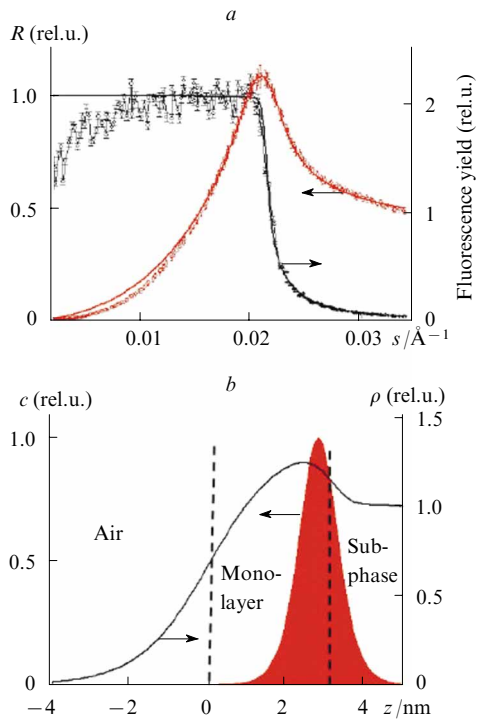


Figure 10. Angular dependences of the X-ray reflectivity (R) and the yield of fluorescence (Zn K_α radiation) (*a*); the depth profiles of the electron density distribution (ρ) and zinc atoms distribution (c) for the monolayer of compound **1** on the liquid surface (*b*); s is the modulus of the wave vector and z is the coordinate along the normal to the monolayer surface.

Orientation of molecules **1** in the monolayer was determined from analysis of the depth profiles of the distribution of zinc atoms and electron density (Fig. 10). It was established that the Zn-containing porphyrin ring does face water; this agreed with the results of molecular modelling and with information obtained during the sample preparation.[59]

Then, the monolayers prepared were transferred onto a silicon substrate. To prepare monolayers with different orientations of molecules **1** with respect to the substrate surface, the monolayers were transferred using the LB and LS techniques. Transfer by the LB method required stabilization of the monolayer with octadecylamine (ODA); therefore, the LB films prepared from monolayers of **1** : ODA mixture (1 : 4 molar ratio) were studied.

Experimental data for the monolayer of molecules of compound **1** transferred onto the silicon substrate using the LS technique are shown in Fig. 11. The transition layers (spread) at the film boundaries were $\sim$0.5 nm thick, which seems to be due to inheritance of the substrate profile. The monolayer thickness averaged over the sample surface was 2.8 ± 0.5 nm. The electron density profile indicates the presence of a lower-density layer between the substrate and the Zn-containing layer, which corresponds to the region between the fullerene and porphyrin. The depth

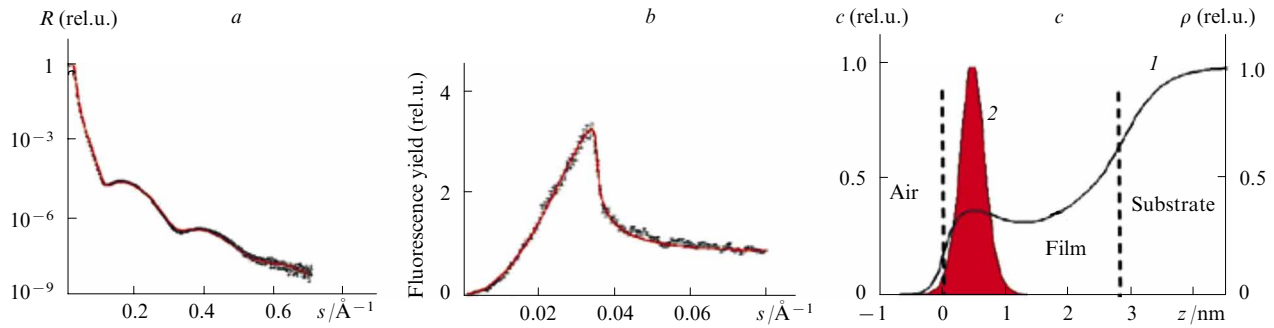


Figure 11. Monolayer of compound **1** transferred onto a silicon substrate by the LS technique.[59] (*a*) Angular dependence of the X-ray reflectivity; (*b*) angular dependence of the yield of fluorescence (Zn K_α radiation); (*c*) the depth profiles of the electron density distribution (*1*) and zinc atoms distribution (*2*) along the normal to the substrate surface.

profile of the distribution of zinc atoms (see Fig. 11 *c*) shows that the zinc-containing porphyrin ring of molecules **1** faces the air/film interface. This molecular orientation corresponds to film transfer using the LS technique.

Consider the structure of a monolayer of **1**:ODA mixture, transferred onto the silicon substrate using the LB technique (Fig. 12). The reconstructed depth profile of the electron density distribution is uniform. This may be due to the presence of ODA molecules. Transition layers at the film boundaries (spread of $\sim$0.5 nm) are due to the substrate profile. The monolayer thickness averaged over the sample surface is 2.8 ± 0.5 nm. Taking into account the presence of transition regions at the film boundaries, this value is consistent with the sizes of molecules **1** and ODA measured along the normal to the substrate surface, found by molecular modelling. The depth profile of the distribution of Zn atoms shows that the porphyrin moieties of compound **1** are closer to the substrate than the fullerene fragments. This corresponds to transfer of monolayers from water surface using the LB technique (from bottom to top). The structure of such films is significantly different from that of the films prepared by the LS method.

The results obtained indicated that preferential orientation of molecules **1** in the films prepared by transfer of monolayers from the surface of the liquid subphase onto solid substrates is retained.

Yet another example of interdisciplinary approach to investigations of interfaces between two compounds is provided by a study[60] on interfaces in Si/Ge multilayer heterostructures prepared by low-temperature molecular beam epitaxy. The samples represented structures comprising four germanium layers separated by silicon layers deposited onto a Si(100) buffer layer 0.2 μm thick. Each silicon layer was 10 nm thick, germanium layers were 2, 3, 5, 7, 10 and 12 monolayers thick, the Ge monolayer thickness being 0.14 nm.

The depth profile of the electron density distribution in the Si/Ge heterostructures obtained after processing the experimental X-ray reflectivity curves is shown in Fig. 13. The experimental angular dependences of the X-ray reflection exhibit superstructure peaks due to periodic structure of the samples. As the thickness of the germanium layers increases, the superstructure peaks at wide angles disappear, probably, due to thickening of the transition layers. All the samples studied were characterized by different number of thickness oscillations between the superstructure peaks. Initially, this was associated by violation in the order of layers; however, transmission electron microscopy studies of such heterostructures revealed no violations except the appearance of the silicon – germanium oxide surface layer. Taking into account this layer in the theoretical model gave better agreement between the calculated and experimental angular dependences. The refined thickness values of the silicon and germanium layers are listed in Table 1.

The depth distribution of germanium atoms in the heterostructures under study (Fig. 14) was obtained by

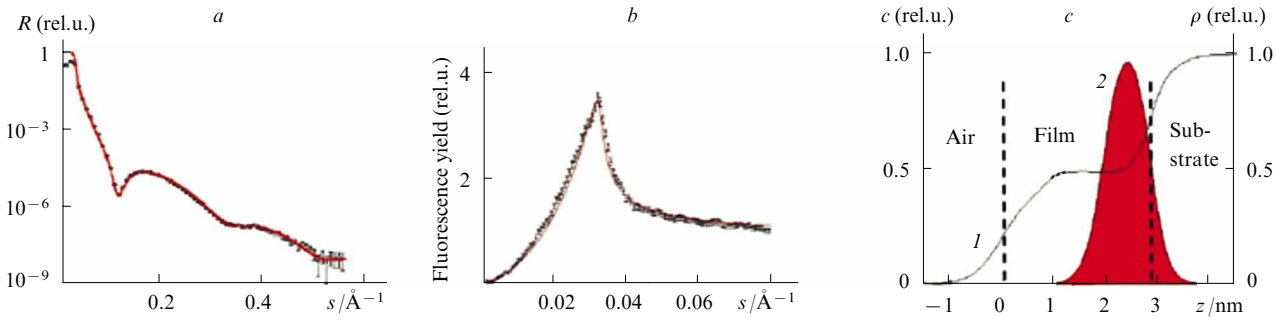


Figure 12. Monolayer of molecules of compound **1** transferred to the silicon substrate by the LB technique.[59] (*a*) Angular dependence of the X-ray reflectivity, (*b*) angular dependence of the fluorescence yield (Zn K_α radiation), (*c*) the depth profiles of the electron density distribution (*1*) and Zn atoms distribution (*2*) along the normal to the substrate.

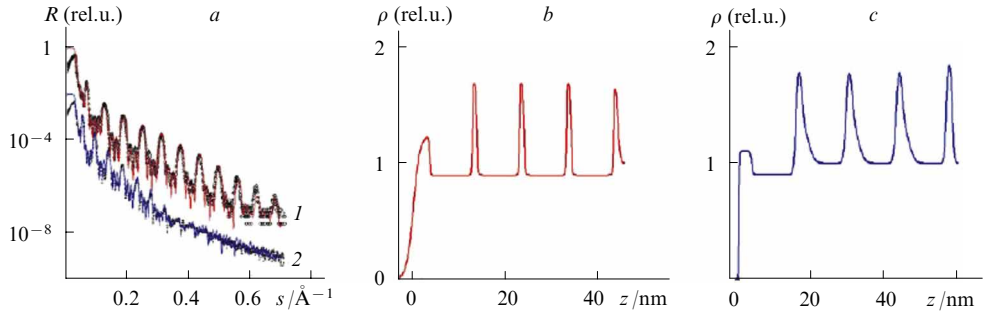


Figure 13. Angular dependences of the X-ray reflectivity for Si/Ge heterostructures with germanium layers 5 (*1*) and 12 (*2*) monolayers thick (*a*) (for clarity, the curves are shifted relative to one another by two orders of magnitude) and the depth profiles of the electron density distribution in the layers *1* (*b*) and *2* (*c*).[60]

Table 1. Germanium and silicon layer thickness from X-ray reflectivity data.[60]

Sample No.	Number of germanium monolayers	Monolayer thickness /nm	
		germanium	silicon
1	2	0.61	9.54
2	3	0.82	10.24
3	5	0.99	9.20
4	7	1.05	11.40
5	10	1.45	9.72
6	12	1.70	12

analyzing experimental data on the fluorescence yield under conditions of total external reflection from Ge atoms. The results obtained confirmed the formation of a Ge-containing near-surface layer in all samples. Changes in the character of interfaces with increasing the thickness of germanium layers were revealed. Samples with the germanium layers from 2 to 10 monolayers thick were characterized by mainly symmetric distribution of silicon in the top and bottom layers. If a layer is less than 12 monolayers thick, its bottom part facing the substrate has a thicker transition layer. X-Ray reflectivity (see Fig. 13), X-ray standing wave (see Fig. 14) and electron microscopy studies showed that as the number of Ge monolayers increases to 12, the boundaries facing the substrate side become of island character.

It should be noted that for all heterostructures the first germanium layer has uniformly diffuse interface (see Fig. 14 *a*,*b*). The sample containing twelve germanium monolayers revealed sharp changes in the character of growth of the subsequent silicon and germanium layers; this manifested itself as high inhomogeneity of the top silicon layer, which increased from one layer to another.

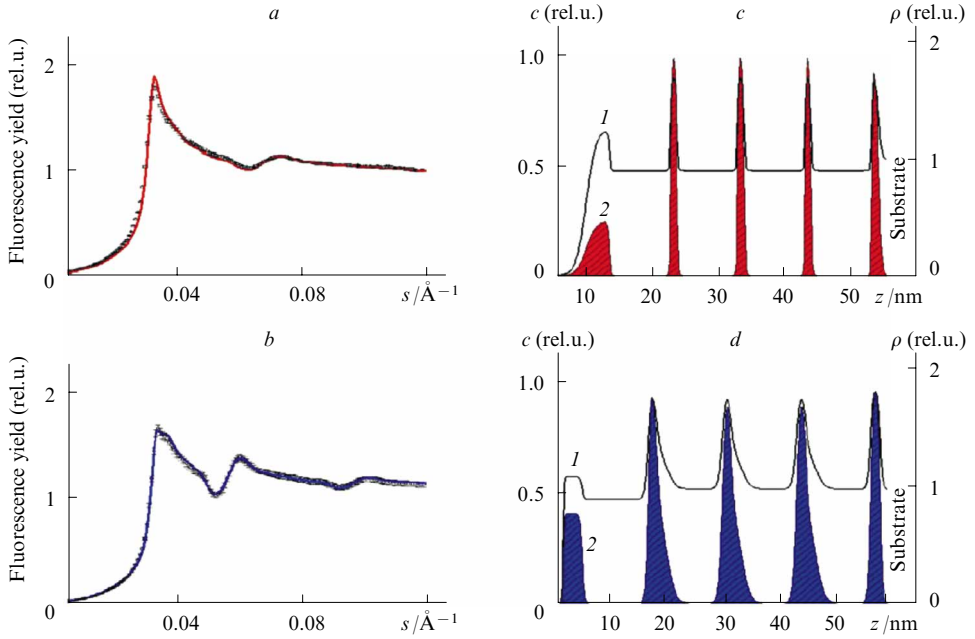


Figure 14. Angular dependences of the fluorescence yield from germanium atoms in Si/Ge heterostructures. Germanium layers are 5 (*a*) and 12 (*b*) monolayers thick and the corresponding depth profiles of the electron density distribution (*1*) and germanium atoms distribution (*2*) (*c*, *d*).[60]

Probably, the 12-monolayer thickness of the germanium layer is sufficient for changing the character of growth of the subsequent silicon layers due to the difference between the lattice constants of silicon and germanium.

Studies on thin-film materials for organic electronics represent an important application of grazing-incidence X-ray diffraction and the X-ray reflectivity method. Some relevant examples are presented below.

III. Oligothiophene derivatives and their application in organic electronics

There is considerable literature concerning organic macromolecular systems that exhibit the properties of semiconductors.[61–64] Such systems may appear to be an alternative to inorganic semiconductors in production of cheap optoelectronic devices, such as organic thin-film transistors (OTFT), light-emitting diodes, photovoltaic cells, lasers, sensors, *etc*.[65–71]

The first conductive polymers were synthesized by MacDiarmid, Shirakawa and Heeger who won the 2000 Nobel Prize in chemistry.[72–74] It was found that π-conjugated polymers [*e.g.*, polyacetylenes, poly-(*p*-phenylenes), polyphenylenevinylenes, polypyrroles, polythiophenes, polyfurans, *etc*.] can exhibit the properties of conductors upon changing the π electron count in specified manner (*i.e.*, on doping). Usually, doping is achieved chemically or electrochemically (redox doping), which leads to formation of a delocalized π-system and, as a result, to significant changes in the electric, magnetic, optical and structural properties of such polymers, in particular, to an increase in the conductivity by a few orders of magnitude. Not only redox doping, but also doping by irradiation, 'injection of charge carriers' or non-oxidative doping is possible. Materials with both n-type and p-type conductivity can be produced by doping.

Devices based on semiconducting polymers do not provide an alternative to the existing inorganic (silicon) electronics, because of lower performance due to a relatively low charge carrier mobility in OTFT, which restricts the operating frequency. However, electronic devices based on inorganic conductors (metals) and semiconductors (*e.g.*, silicon) are produced using complicated technologies including etching or lithography that involve high-temperature treatment, which makes these devices much more expensive. At the same time, semiconducting and conductive organic macromolecular systems combine the advantages of plastics (low weight, transparency and flexibility) with simplicity of production.

Recently, there has been search for novel conjugated organic structures with high charge carrier mobility, conductivity, luminescence efficiency and good processability from solutions in order to design more efficient materials and technologies for organic optoelectronics.

Thiophene-containing oligomers and polymers combine unique properties including effective electronic conjugation, chemical stability and synthetic variability. The last-mentioned feature can serve to control the properties by derivatization of these compounds.[75] The most striking examples of such derivatives are provided by a complex of poly(3,4-ethylenedioxythiophene) with polystyrene sulfonate (PEDOT-PSS) and poly(3-hexylthiophene) (P3HT).[76,77] These compounds are produced on a large scale. The complex, PEDOT-PSS, exhibits a uniquely high conductivity (10^2–10^3 S cm^{-1}) while P3HT is a conventional p-type semiconductor for OTFT and serves as electron-donor material in organic solar cells.[78] The major drawback of P3HT is a relatively low oxidation potential. This leads to doping of the compound in air and, as a consequence, to the need for thorough protection of organic electronics devices from oxygen and atmospheric moisture using additional multilayer protective coatings. Thus, the corresponding production technology thus becomes more expensive. In this connection, the design of novel semiconductor materials with improved chemical stability and electrochemical oxidation stability is of great importance for progress in modern organic electronics.

Solubility enhancement of such systems, morphology control of thin films prepared from them and preservation of semiconductor properties of the thin films are also topical. These problems are rather complicated and contradictory, becasuse the higher the degree of crystallinity of a compound the better the semiconductor properties[79] and, *vice versa*, high solubility and quality are usually typical of thin films of amorphous compounds. In the case of OTFT, a vital task is to decrease the thickness of semiconductor films because only the first one or two monolayers merely 3–5 nm thick are involved in the operation.[80,81] Organic transistors with stable operating properties are usually produced from films 30–100 nm thick, which is due to inhomogeneity of coatings. This leads to at least tenfold excess consumption of valuable semiconductor materials and increases the cost of the devices.

III.1. The structure of α,α′-dialkylquaterthiophenes and their carbosilane multipods

To solve these problems in organic electronics, researchers at the Enikolopov Institute of Synthetic Polymeric Materials, Russian Academy of Sciences, for the first time used novel organic and organosilicon conjugated compounds based on oligothiophenes and oligothiophenephenylenes. The available synthetic methods make it possible to obtain two fundamentally different classes of oligothiophene-containing dendrimers and their analogues (Fig. 15), namely, compounds with oligothiophene moieties at the periphery (items *4*, *8*, *11*, *13*) or in the bulk of the dendritic macromolecule; in the latter case, one deals with oligothiophene-silane monodendrons (items *1–3*), dendrimers (items *9*, *10*), dendronized polymers (item *12*), as well as their linear (item *3*) and branched (items *5–7*) analogues.

Studies of the impact of the molecular structure, topology and degree of branching of such systems on their phase behaviour and bulk structure, as well as on the morphology and electrical properties of thin films prepared from them is an important problem in basic research. Optimization of the molecular structure makes it possible to synthesize compounds which combine the semiconductor properties of the parent oligothiophenes with the solubility and good film-forming properties typical of polymers.

A comparative analysis of the structure and phase behaviour of monomers, dimers and tetramers based on α,α′-dialkylquaterthiophenes allows one to establish correlations between the molecular structure, phase behaviour of a compound and its physical and electronic properties. Aliphatic periphery in these compounds can either stabilize or destabilize the molecular packing of quaterthiophenes.[82] For all compounds studied, the packing parameters of quaterthiophenes are close to those of the 'herring-bone'-

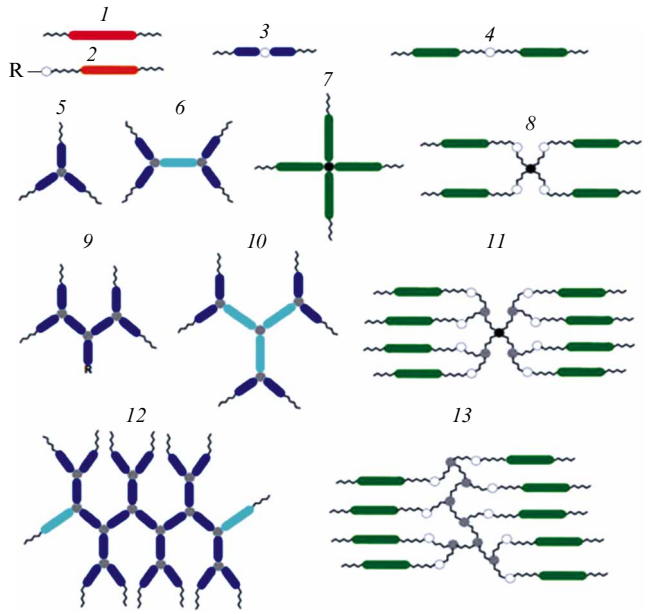


Figure 15. Various structural types of systems under study. Topology: linear (*1* – *4*), branched (*5* – *8*) and dendritic (*9* – *13*).

packed polythiophene (samples with linear aliphatic groups). The samples with branched alkyl chains exhibit a distorted packing of oligothiophene blocks due to the need for incorporation of bulky substituents into the crystal structure of the material. For a centrosymmetric unit cell of oligothiophenes the 11th (d_1) and 20th (d_2) reflections are the most intense. Assuming that the projection of the sublattice on the plane normal to the molecular axis is almost orthogonal, the unit cell cross-section (s) can be calculated as follows:

$$s = \frac{4\,d_2^2 d_1}{\sqrt{4\,d_2^2 - d_1^2}} \qquad (59)$$

A comparison of the s values, experimental density of the samples and charge carrier mobility values measured for thin-film transistors [see Table 2; for complete analysis, data for unsubstituted quaterthiophene (4T) and polythiophene are also presented] suggests the following. First, chains in the compounds with linear substituents are packed more densely than in the analogues with branched aliphatic fragments. Next, for the compounds with linear substituents the surface area per chain decreases in the series of compounds **3** – **6** – **8** – **4**. This is probably due to an increase in the driving force for segregation between the thiophene and alkyl blocks. Yet another reason is the presence of a liquid-crystalline phase with increased mobility of molecules in the dimer and tetramer in the course of cooling from the isotropic state prior to crystallization. Annealing in the liquid-crystalline phase enables significant structural rearrangements of molecular fragments relative to one another and, correspondingly, a considerable increase in the degree of crystallinity on subsequent cooling. A similar effect was reported for partially crystalline polymers that crystallize in the mesophase. For instance, when cooling from the rotation-crystalline phase, the degree of crystallinity of flexible-chain polymers [polyethylene, poy(dialkylsiloxane)] can approach 100%.[83 – 85]

Structures 2 – 8

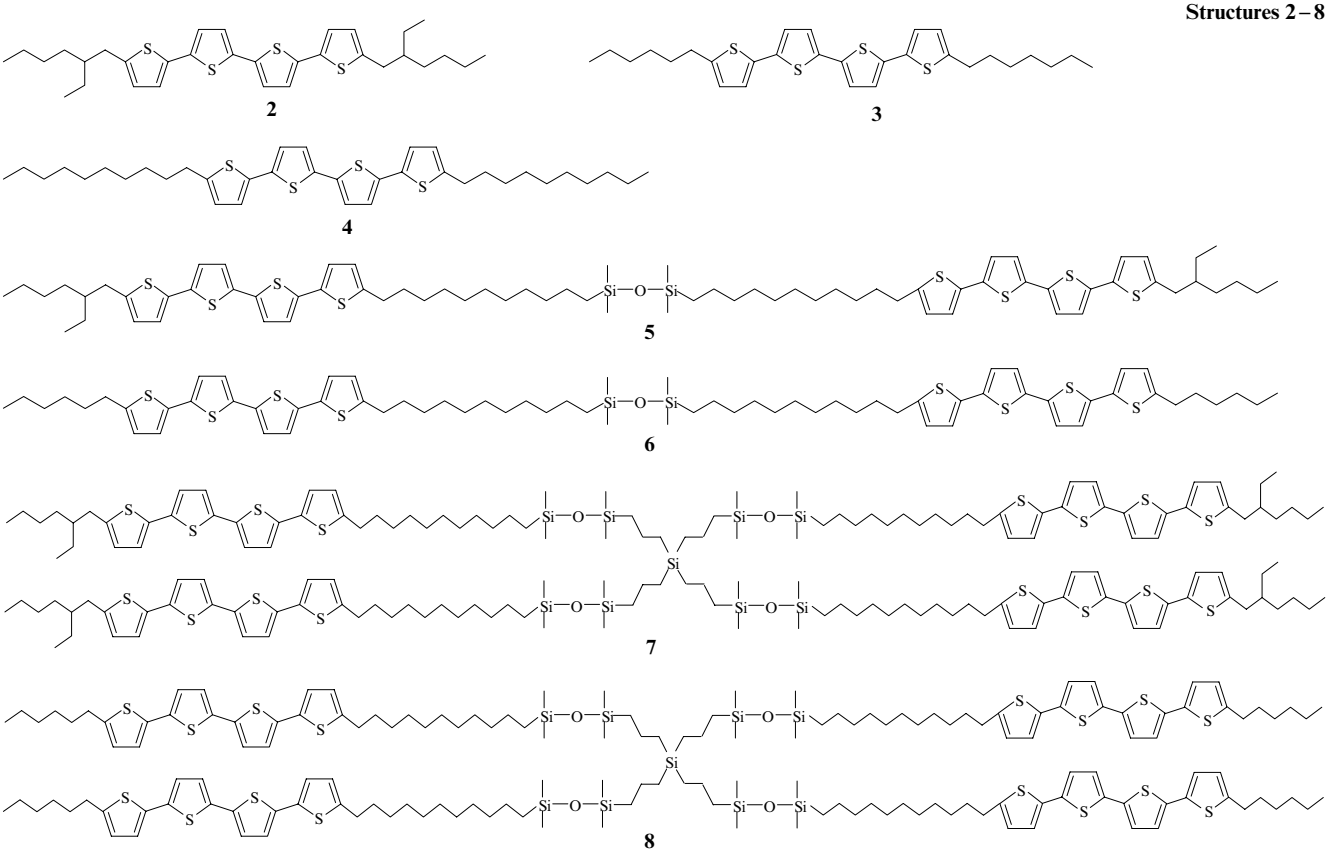


Table 2. Packing efficiency of quaterthiophene blocks and charge carrier mobility.[82]

Compound	ρ_{exp} /g cm^{-3}	d_1 /Å	d_2 /Å	s /Å^2	Tilt angle [a] /deg	Charge carrier mobility /cm^2 V^{-1} s^{-1}
4T (Ref. 86)	–	4.55	3.93	43.0	26	0.0001
Polythiophene (Ref. 87)	–	4.52	3.90	43.2	–	–
2	1.15	4.63	3.94	44.1	58	–
3 (Ref. 83)	1.19	4.59	3.91	43.2	22	0.02
4	1.15	4.50	3.89	42.0	22	0.1
5	1.12	4.66	4.04	45.1	43	–
6	1.08	4.53	3.99	43.0	15	0.003
7	1.11	4.68	4.05	45.5	< 25	0.0004
8	1.12	4.56	3.86	42.7	< 20	0.02

[a] The tilt angle of quaterthiophene moieties was calculated relative to the 100 direction.

In contrast to compounds with linear end groups, the surface area per chain increases in the series of compounds **2**–**5**–**7** owing to kinetic reasons. We believe that crystallization of substituted oligothiophenes occurs in a number of steps characterized by different degrees of ordering:

— isotropic melt;
— partially ordered smectic phase;
— partially disordered thermotropic crystal; and
— thermodynamically stable crystalline phase.

Therefore, the final structure of a material depends strongly on the thermal prehistory of the sample. Clearly, the presence of branchings (a kind of topological defects) slows down the local reorganization. Conventional methods for preparation of samples including extrusion do not always lead to formation of the equilibrium crystalline phase. Finally, the sample may contain a mixture of stable and unstable polymorphs, which strongly complicates the phase analysis. In the mesomorphic state, materials can form large monodomains (to hundreds of micrometres in size), which is important for fabrication of OTFT with reproducible properties. Therefore, an optimum chemical structure should ensure a balance between the dense packing of thiophene blocks and the ability of the material to undergo self-assembly in the liquid-crystalline phase.

The highest charge carrier mobility equal to 0.1 cm^2 V^{-1} s^{-1} was obtained for quaterthiophene **4** with long decyl groups (the smallest unit cell cross section is 42.0 Å^2) while the lowest mobility (0.0004 cm^2 V^{-1} s^{-1}) was obtained for tetramer **7** with branched 2-ethylhexyl groups and a largest unit cell cross section of 45.5 Å^2. The absence of measurable charge carrier mobility in dimer **5** can be explanied by not only low s value, but also large inclination of the quaterthiophene units (43°). An increase in the tilt angle of oligothiophenes used in the semiconductor devices is undesired because in this case the charge carrier injection from contacts becomes inefficient. Presumably, the large tilt angle of the semiconducting oligothiophene blocks precludes efficient charge carrier injection from contacts and the energy barrier between domains with different orientations in the polycrystalline film increases.

In the quaterthiophenes with linear hexyl and decyl groups (**3** and **4**, respectively) the s value decreases from 43.2 to 42.0 Å^2, which corresponds to an increase in charge carrier mobility from 0.02 to 0.1 cm^2 V^{-1} s^{-1}. Similarly to this, a decrease in s from 45.5 to 42.7 Å^2 for tetrapods **7** and **8** containing branched 2-ethylhexyl and linear hexyl groups is accompanied by an increase in charge carrier mobility from 0.0004 to 0.02 cm^2 V^{-1} s^{-1}. This implies a correlation between the calculated unit cell cross-section and the charge carrier mobility.

Thus, the chemical structure of the alkyl periphery plays an important role in the molecular packing and thermal stability of the ordered phase. For quaterthiophenes with linear end groups the temperature of the transition from the crystalline to the partially ordered state derceases as the aliphatic groups elongate. Moreover, alkyl chains can be destabilized by introducing branching points of different nature. For instance, the molecules of quaterthiophenes with 2-ethylhexyl groups adopt a zigzag conformation in the crystalline state at room temperature. Conformational variations lead to appreciable changes in the energy of the polymorphic transition and isotropization temperature.

III.2. Thin films of quinquethiophene derivatives prepared by different methods: a comparative analysis

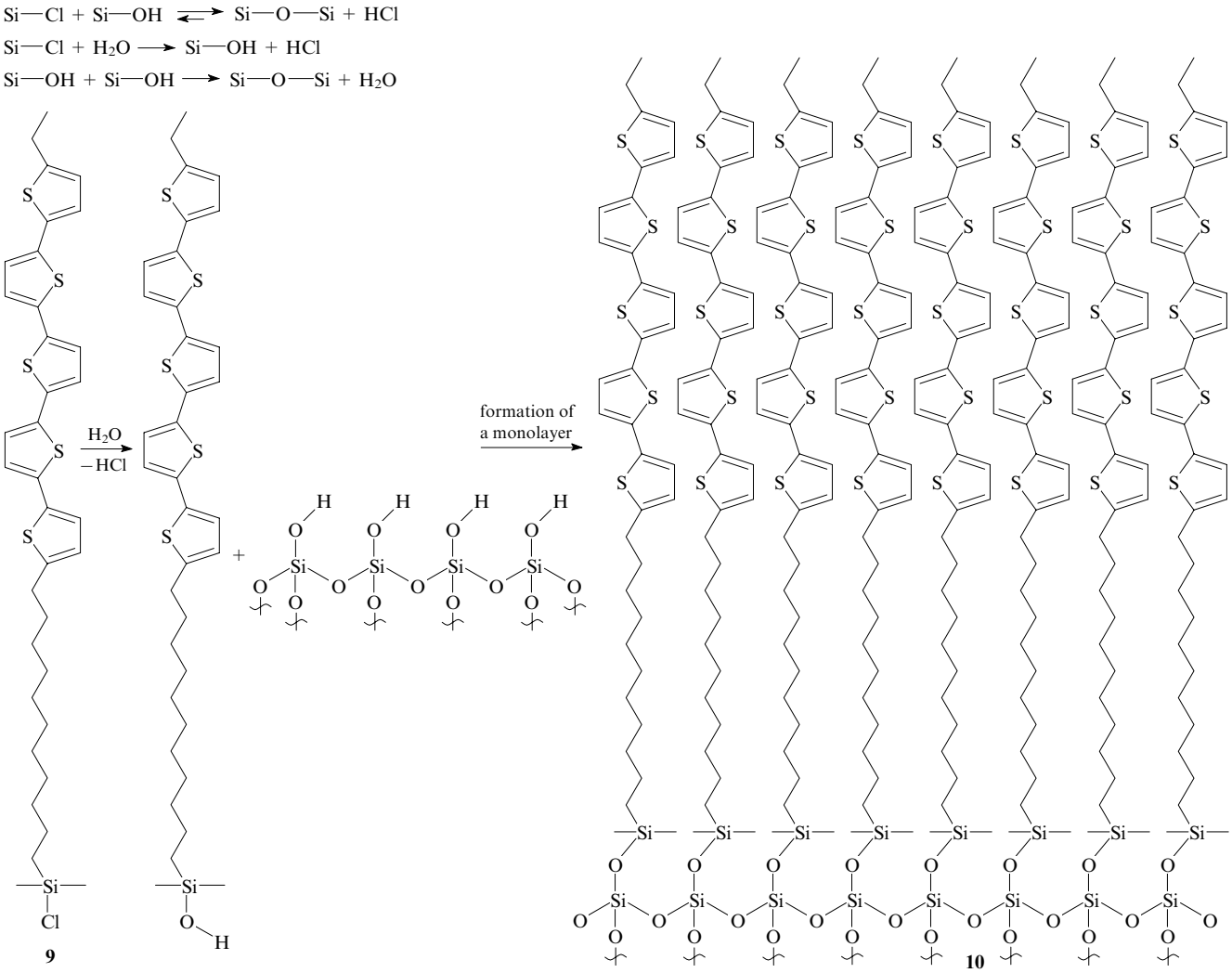
Relatively fast preparation of self-assembling thin organic semiconducting films is possible by the LB technique, by spin coating, and by casting.[88,89] This was done with chloro[11-(5‴″-ethyl-2,2′:5′,2″:5″,2‴:5‴,2⁗-quinquethiophene-5-yl)undecyl]dimethylsilane (quinquethiophenechlorosilane **9**) as precursor. Compound **9** forms stable chemical bonds with the activated surface of silicon substrate owing to high reactivity of the chlorosilane group (Scheme 1).

The structure and supramolecular organization of coatings **10** were studied by X-ray reflectivity (Fig. 16) and grazing-incidence X-ray diffraction. Reconstruction of the electron density in the direction perpendicular to the film plane showed that monolayers are comprised of two sublayers characterized by different electron density values.

One sublayer, the closest to the silicon substrate (ρ_e = 0.67 e Å^{-3}), represents the aliphatic zone, and has low electron density (ρ_e = 0.342 e Å^{-3}), whereas the distant sublayer with much higher electron density (ρ_e = 0.566 e Å^{-3}) contains quinquethiophene moieties. Good electronic properties of these films are due to dense packing of oligothiophene moieties. Experimental data agree with the theoretically calculated reflectivity curves.

Changes in the monolayer structure with increasing the transfer surface pressure are illustrated in Fig. 17. A comparison of structural parameters of sublayers obtained at different pressures taking into account geometric considerations and results of molecular modelling (the contour

Scheme 1



length of quinquethiophene and undecyl fragments is 19.8 Å and 13.3 Å, respectively) showed an increase in the thickness of the oligothiophene region with increasing surface pressure owing to a decrease in the oligothiophene tilt to the normal plane from 22 to 13°. The thickness of the aliphatic zone remains almost unchanged.

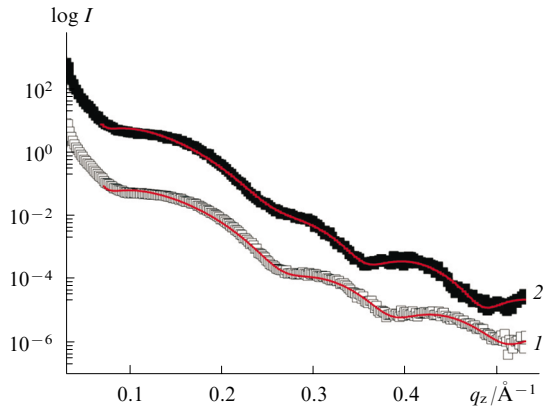


Figure 16. X-Ray reflectivity curves for LB films prepared from a solution of compound **9** (concentration 0.33 g litre^{-1}) at pressures of 30 (*1*) and 40 mN m^{-1} (*2*).[89]
For convenience, curve *2* is shifted along the ordinate axis. Red curves denote the best stochastic fit.

It should be noted that a tilt angle of about 13° was observed after annealing of the monolayer prepared from a solution of the same compound in toluene, whereas no inclination of the quinquethiophene moieties was observed in the freshly prepared self-assembled monolayer. It follows that the LB technique makes it possible to attain a high surface coverage and to reduce the tilt angle of thiophene blocks to the substrate surface no increasing the surface pressure. This is of paramount importance for the onset of high electronic properties

Films **10** prepared by spin coating showed the best crystal structure (highest surface coverage) at a solution concentration of 0.6 g litre^{-1}. The 2D grazing-incidence X-ray diffraction patterns of these films demonstrate three Bragg reflections (Fig. 18) corresponding to interplanar spacings of 4.505, 3.893 and 3.142 Å, which is characteristic of the herringbone packing of polythiophenes. A weak narrow circular reflection (d = 4.134 Å) is due to uncovered substrate surface. It should be noted that spin coating leads to formation of large islands which do not cover a large proportion of the substrate surface (Fig. 19).

This conclusion can be drawn not only using the X-ray structural data, but also from the characteristic shape of the

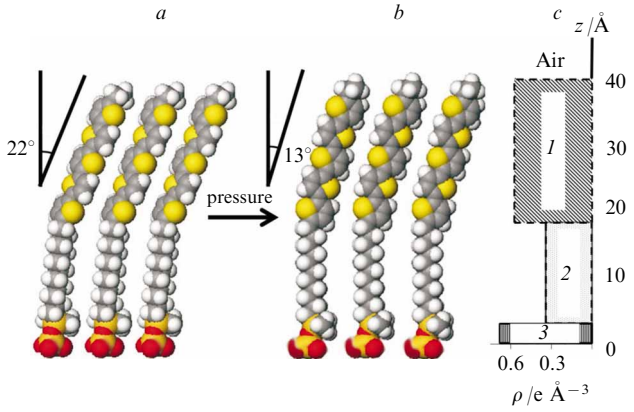


Figure 17. Molecular models for LB monolayer at a pressure of 30 (*a*) and 40 mN m^{-1} (*b*) and the electron density distribution along the normal (*z* axis) to the substrate surface (*c*).[89] Quinquethiophenes (*1*), aliphatic fragments (*2*) and substrate (*3*).

reflectivity curve (see Fig. 18 *c*) which clearly demonstrates a Bragg reflection. Such a broad peak originates from stacked monolayers that form large pyramidal islands on the substrate surface. The monolayer height calculated from the position of the Bragg reflection is ~40.5 Å, which agrees with the thickness of the films prepared by the LB technique. Therefore, the LB technique under optimum conditions makes it possible to prepare films with almost 100% surface coverage and almost orthogonal orientation of the molecules in the monolayer **10**. However, it should be noted that multilayer films can be prepared using not only functionalized chlorosilane molecules, but also non-functionalized molecules, such as α,α′-dialkyloligothiophenes. Moreover, the chemically reactive part of the film **10** prepared by spin coating can contain nonhydrolyzed chlorosilane groups, which may deteriorate its electrical properties.

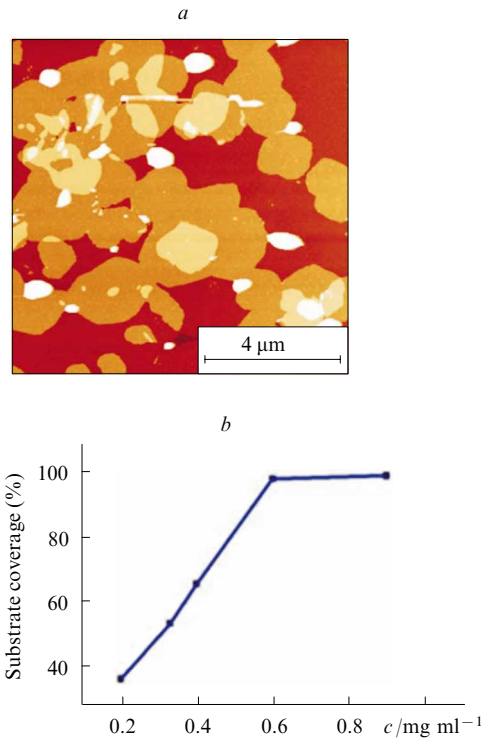


Figure 19. AFM image of thin films on a silicon substrate prepared by spin coating (700 rpm) from a solution of compound **9** in toluene (0.6 mg ml^{-1}) (*a*), and the dependence of the substrate area covered with the oligothiophene on the concentration of the initial solution (*b*).[89]

Summing up, the LB technique is promising for the preparation of highly ordered monolayers of organosilicon functionalized quinquethiophenes with vertical orientation of thiophene moieties relative to the substrate surface. The

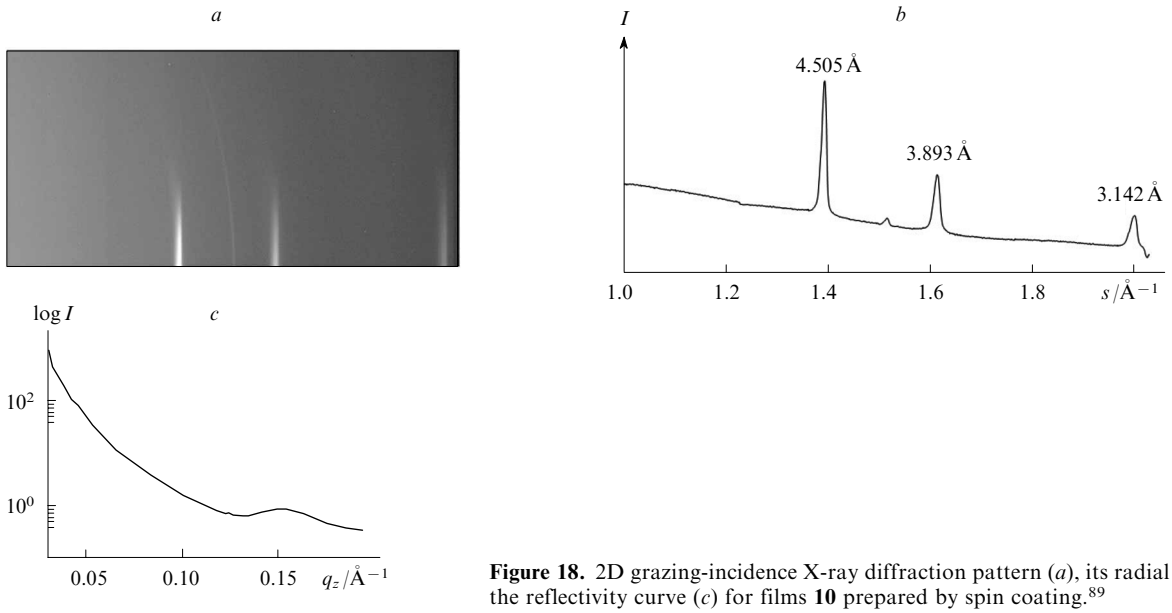


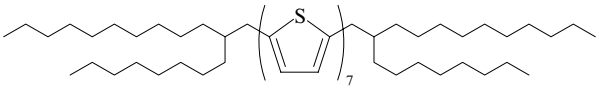
Figure 18. 2D grazing-incidence X-ray diffraction pattern (*a*), its radial scan (*b*) and the reflectivity curve (*c*) for films **10** prepared by spin coating.[89]

cast and spin coating techniques do not provide full and uniform coating of the substrate.

III.3. Structure of α,α′-bis(2-octadodecyl)septithiophene thin films prepared using the Langmuir–Blodgett technique

The solubility of compounds based on oligothiophenes decreases as aromatic fragments elongate (see above). At the same time, going to higher oligothiophene derivatives and corresponding increase in the conjugation length are accompanied by significant improvement of the conductive properties of materials. Introduction of branched aliphatic substituents into the molecular structure leads to improvement of the film-forming properties of the material; therefore, studies on the phase behaviour and structure of thin films prepared from long-chain α,α′-dialkyloligothiophenes become topical. Some results will be considered below taking α,α′-bis(2-octadodecyl)septithiophene (**11**) as an example.

Structure 11



11

Strong π–π-interaction between molecules of this compound and phase separation between the rigid conjugated backbone and long flexible chains at the periphery leads to the existence of the liquid-crystalline phase. Indeed, the DSC thermogram of septithiophene (Fig. 20) shows three reversible transitions, *viz*., a low-temperature transition at 65 °C (ΔH = 9.0 J g^{-1}), a high-temperature transition at 166 °C (ΔH = 39.0 J g^{-1}) and isotropization (clearing transition) of the sample at 171 °C (ΔH = 9.4 J g^{-1}). The value of the enthalpy of melting suggests that the compound was in the liquid-crystalline state prior to isotropization. An analysis of the X-ray diffraction patterns of the fibres obtained at different temperatures (see Fig. 20 *d*–*f*) showed that at low temperatures the compound crystallizes in the triclinic system with the following unit cell parameters: a = 36.8, b = 8.90, c = 11.34 Å, α = 90, β = 80.4, γ = 72°; the unit cell volume is V = 1769.3 Å^3 and the calculated density is ρ = 1.07 g cm^{-3}. The most intense equatorial peak with fifth-order reflections is characteristic of a well-ordered layered structure. The 100 interlayer spacing is 34.3 Å, which is much smaller than the length of molecule **11** in the fully extended conformation (49 Å).

Thus, one can assume that molecules of the compound under study are highly tilted relative to the normal to the layer surface. The tilt angle was evaluated from the results of reconstruction of the electron density distribution using the relative scattering intensities for different orders of the fundamental reflection (see Fig. 20 *b*,*c*). It was found that the thickness of the sublayers with high and low electron density, corresponding to the thiophene core and alkyl substituents, is 22.8 and 11.5 Å, respectively. Therefore, the thiophene core is tilted by 15° to the layer plane. Bulky alkyl substituents make the packing density of the thiophene blocks less dense than in systems with linear alkyl chains.

The first phase transition at 65 °C corresponds to a crystal–crystal transition and occurs with retention of lattice symmetry. At 100 °C, the unit cell remains triclinic with the following parameters: a = 36.4, b = 9.73, c = 6.11 Å, α = 90, β = 75.2, γ = 65.9°, V = 1869.0 Å^3 and

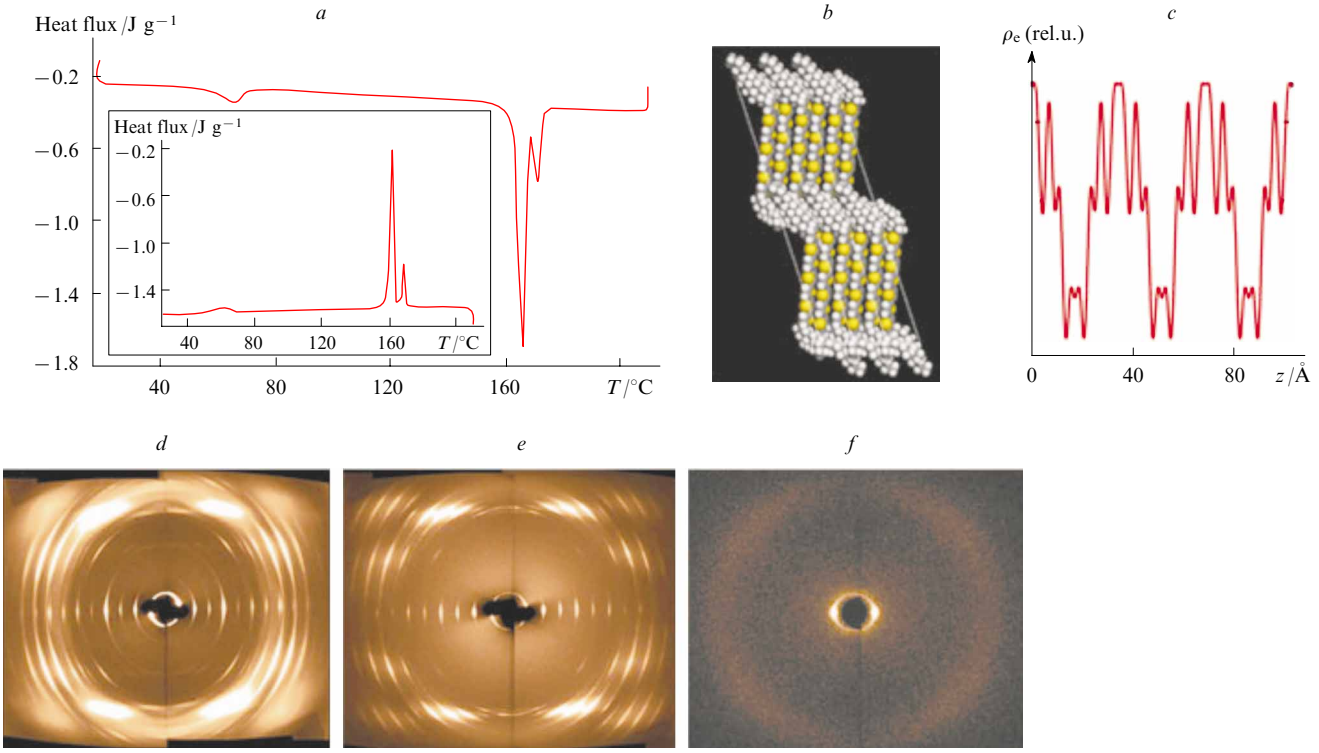


Figure 20. DSC thermogram of compound **11** (inset: cooling curve) (*a*), *ab* plane of the unit cell of **11** at room temperature (*b*), electron density profile along the {100} direction (*c*), X-ray diffraction patterns at 23 (*d*), 100 (*e*) and 168 °C (*f*); the fibre axis is vertical.[90]

$\rho = 1.01$ g cm^{-3}. However, a minor contraction of the unit cell parameters above 65 °C leads to reorganization of molecules in the unit cell; that is why strong, broad off-meridian reflections split into well-defined narrow reflections. In the temperature range of 166–171 °C, the compound is in the liquid-crystalline state and forms a smectic mesophase with an interlayer distance of 33.6 Å.

Relatively high solubility of septithiophene **11** (saturation concentration is 3 g litre^{-1} in toluene) is due to the presence of long-chain branched alkyl substituents. This saturation concentration is sufficient to prepare films a few nanometres thick. An STM study revealed a highly homogeneous morphology of the films even at high magnification. The molecules form a layered structure with a step height of 34 Å. This value is close to 100 interlayer spacing in the bulk material, as was obtained by X-ray diffraction analysis. Therefore, in the thick film, layers are arranged almost normal to the substrate surface.

To form an adsorbed monolayer, one should thoroughly control the substrate surface coverage. Roughness of grain boundaries can be reduced and large 2D single crystals can be obtained provided low nucleation density and rather high seed growth rate. Unsubstituted oligothiophenes often exhibit a tendency to form 3D layered islands prior to completion of the monolayer. The formation of islands without a closed monolayer is observed rarely; usually, the formation of a monolayer is followed by the formation of islands.

Septithiophene **11** is characterized by a linear increase in the surface density of monolayer islands with increasing the solution concentration (Fig. 21 *a*); the increment depends strongly on the surface energy and synthesis conditions (*e.g.*, spinning velocity of the substrate and evaporation rate of the solvent). A complete monolayer was formed on a SiO_2 surface from toluene at a solution concentration of 0.9 g litre^{-1}. The average island size was about 1–2 μm. Above this concentration, the septithiophene molecules tend to form multilayers with an interlayer distance of 34 Å. The rectangular shape of islands indicates their crystalline nature. The high-resolution AFM images of the surface resolve inner periodicity of ~50 Å (see Fig. 21 *b–d*). In the case of multilayer surface coverage, this feature becomes difficult to detect, probably, because of coarsening of domains. This superstructure may result from 2D aggregation of molecules. Indeed, in the case of 3D packing, septithiophene **11** crystallizes in multilayers with partial interpenetration of alkyl chains while the thiophene cores are tilted to the surface. However, in the text below we will show that the tilt angle of molecules in a monolayer is larger than in the 3D crystal. Probably, the surface forces and insufficient interpenetration lead to an increase in the tilt angle and subsequent weakening of the π–π interaction. Thus, the formation of such a superstructure can be due to a balance between geometric factors and intramolecular interaction.[90]

The structure of a monolayer of septithiophene **11** was studied by the method of X-ray reflectivity using four samples. Three films were prepared by spin coating with initial solution concentrations of 0.5, 0.9 and 1.0 g litre^{-1} and the fourth sample was spun from a 0.9 g litre^{-1} solution and then annealed. Experimental data were compared with results of theoretical modelling of the reflectivity curves based on the three-component model (Fig. 22). The best fit obtained for the annealed sample indicated the correctness of the model. The electron density values were 0.43 e Å^{-3} for the thiophene layer and 0.27 and 0.29 e Å^{-3}

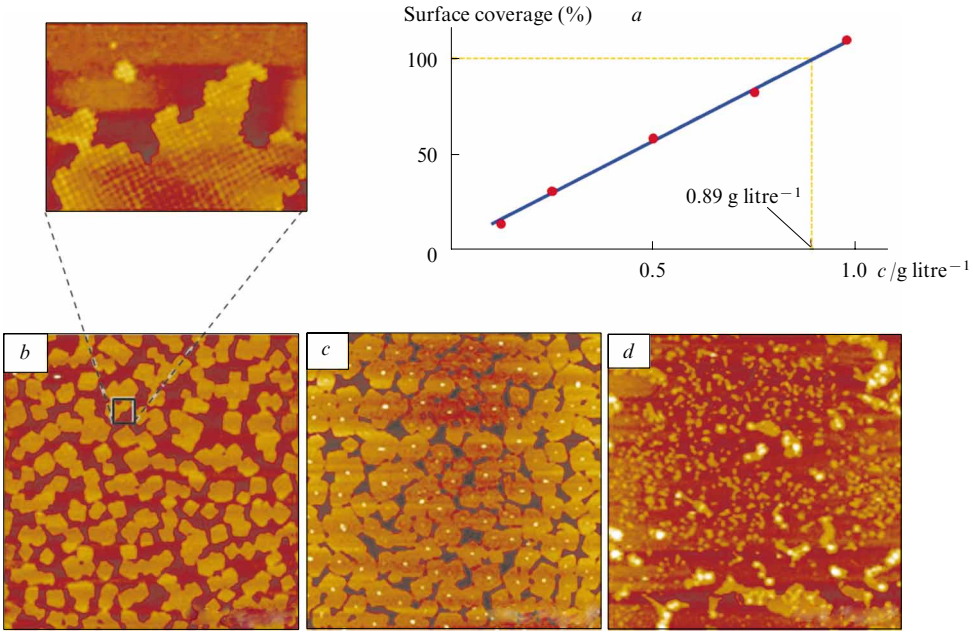


Figure 21. Plot of surface coverage *vs.* solution concentration (*a*), the surface coverage was estimated from scanning force microscopy data; AFM images of the monolayer (*b–d*).[90]
Changes in the monolayer morphology depending on the solution concentration are noticeable. Islands in the submonolayer have a nearly square shape; the inset in Fig. *b* exhibits a superstructure of islands with a period of about 50 Å. AFM images (*b–d*): 12 × 12 μm^2. Solution concentration /g litre^{-1}: 0.5 (*b*), 0.75 (*c*) and 1.0 (*d*).

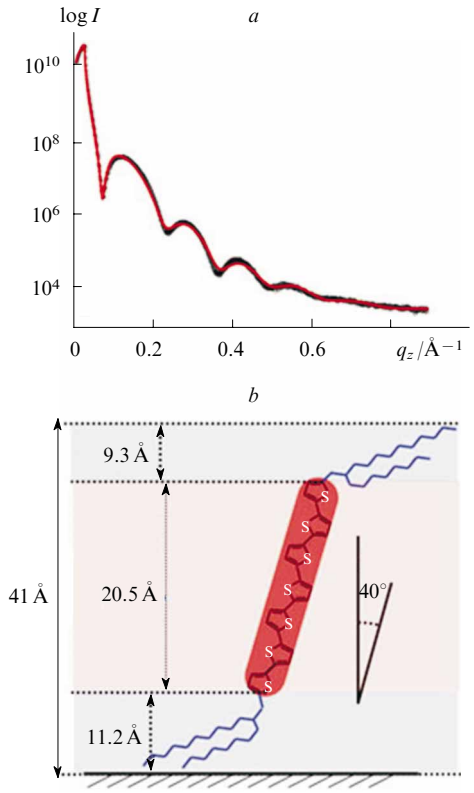


Figure 22. X-Ray reflectivity data for monolayers of compound **11** (*a*) and scheme of the monolayer structure (*b*).[91]

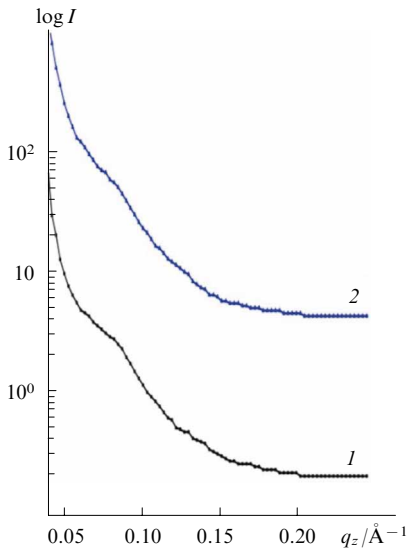


Figure 23. X-Ray reflectivity curves for the Langmuir films of compound **6** prepared at a surface pressure of 8 (*1*) and 25 mN m^{-1} (*2*).

for the top and bottom alkyl layers, respectively. The thickness of the thiophene layer was 20.5 Å, and 9.3 and 11.3 Å for the alkyl layers; the roughness between the layers was nearly 2 Å. Having known the layer thicknesses and the lengths of the corresponding molecular fragments, one can calculate the tilt angles of the thiophene units and alkyl groups to the substrate surface normal (see Fig. 22). For the annealed sample, the tilt angle of the oligothiophene moiety was $\sim 40^\circ$.

Summing up, septithiophene **11** can form crystalline and liquid-crystalline phases. In the 3D case, compound **11** crystallizes in multilayer stacks with partial interpenetration of alkyl chains, while the thiophene cores are tilted to the layer plane. However, the tilt angle of the molecules in a monolayer is larger than in the 3D crystal. In the presence of bulky side substituents the solubility improves and solution deposition of the material and self-assembly of a conducting monolayer become possible.

III.4. Structure of films formed by carbosilane dimers based on α,α′-dialkylquaterthiophenes

Consider the formation of thin films of oligothiophene **6**. It is characterized by one of the highest charge carrier mobility values (see Table 2). Uniform, homogeneous films were prepared by the LB method. An AFM study of the films transferred onto solid substrates at different surface pressures (π = 8 and 25 mN m^{-1}) revealed a film thickness of 4.5 nm. The reflectivity data were analyzed with the StochFit software package which uses stochastic methods for solving the inverse scattering problem. Besides, the electron density distribution curves

$$\rho = \frac{2\pi\delta}{\lambda^2 r_e}$$

thus obtained (δ is the dispersion, r_e is the classical radius of electron equal to 2.814×10^{-5} Å) were represented as three zones of different thickness with a constant electron density within each zone, the zones being separated by surfaces of different roughness. Intensity calculations for such films were carried out according to Parratt, which made it possible to evaluate the correctness of a particular splitting of the electron density distribution curve.

The reflectivity curves of the films of compound **6** (Fig. 23) exhibit two weak minima corresponding to a layer thickness of 45.5 Å. Since half the length of the fully extended molecule **6** is 43.2 Å, one can assume that the monolayers are formed as a result of self-assembly of such units attached to the silicon substrate through siloxane moieties. Thus, clearly, the molecules of compound **6** in the monolayer are most often folded in half.

As mentioned above, the driving force for self-assembly of the Langmuir films of the compound under study is $\pi - \pi$ interaction of oligothiophene fragments, which leads to formation of a 2D rectangular centred lattice whose parameters are close to those of the polythiophene lattice.[92] The grazing-incidence X-ray diffraction patterns for the Langmuir films prepared at a surface pressure of 25 mN m^{-1} (Fig. 24) exhibit the development of a 2D crystal lattice with a = 7.96 and b = 5.65 Å. The interplanar spacings calculated from the observd reflections and the lattice constants of thin films of the compound studied, bulk samples of the material,[82] and crystalline polythiophene are listed in Table 3.

A comparative analysis of the results obtained makes it possible to draw some important conclusions. The a value is the same for both thin films and bulk state of the compound under study. It is larger than for pristine polythiophene owing to the influence of aliphatic fragments. At the same time, the b value is almost unchanges in the bulk state of

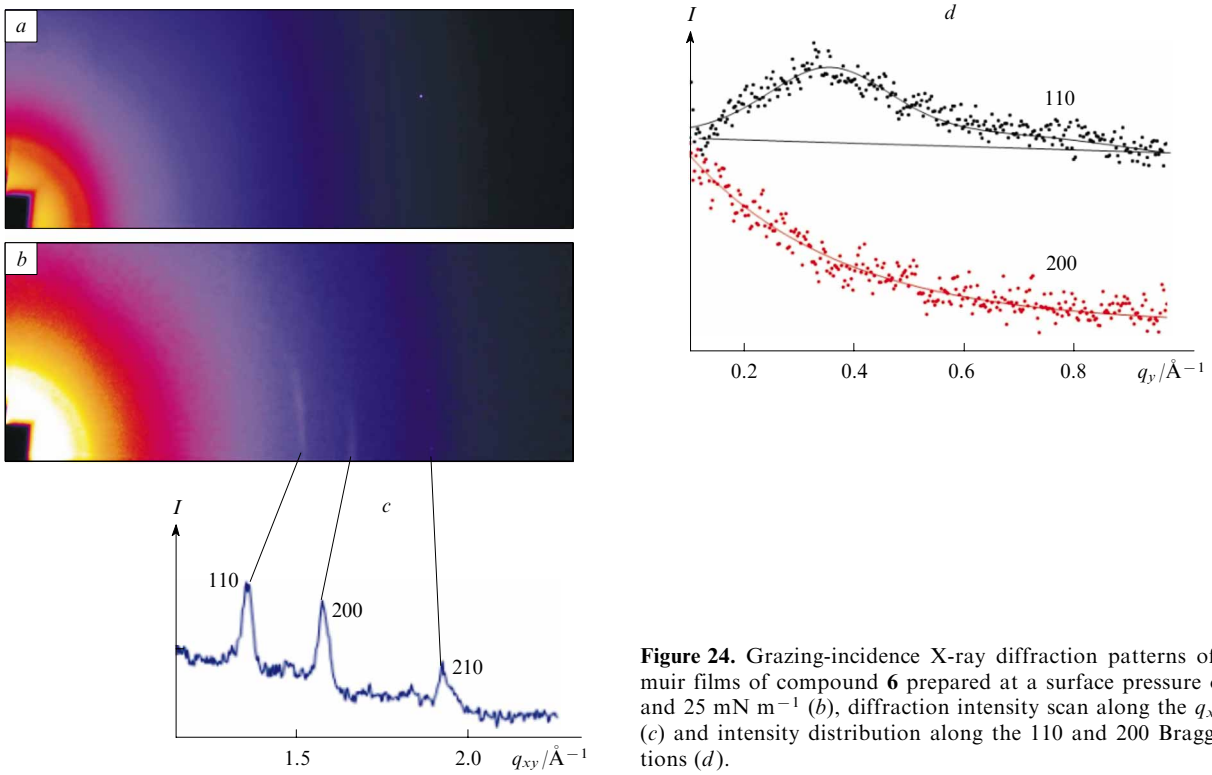


Figure 24. Grazing-incidence X-ray diffraction patterns of Langmuir films of compound **6** prepared at a surface pressure of 8 (*a*) and 25 mN m^{-1} (*b*), diffraction intensity scan along the q_{xy} plane (*c*) and intensity distribution along the 110 and 200 Bragg reflections (*d*).

Table 3. Interplanar spacings (*d*) and lattice constants of thin films of **6**, bulk sample of compound **6** and polythiophene.

Sample	*d*/Å			Lattice constant /Å	
	d_{110}	d_{200}	d_{210}	*a*	*b*
Thin films	4.63	3.99	3.27	7.98	5.69
Bulk sample	4.53	3.99	3.23	7.98	5.52
Polythiophene	4.52	3.92	3.19	7.83	5.52

material **6** and polythiophene, being 3.1% larger for the thin films.

This can be explained by comparing the angular width of the 110 and 200 Bragg reflections (see Fig. 24 *d*). The 200 reflection is almost perpendicular to the *q* axis, whereas the 110 reflection is highly tilted to this axis. Thus, in the thin film when the crystal lattice is observed along the vector **a**, the quaterthiophene moieties are perpendicular to the substrate surface and their tilt director is almost aligned with the vector **b**. The tilt angle is 14°, being close to that of the quinquethiophene moieties in thin films of **10**[89] (see above). Besides, calculations of the change in the parameter *b* from the observed tilt of oligothiophene moieties give

$$\frac{\Delta b}{b} = \left(\frac{1}{\cos\varphi} - 1\right) \times 100 = 3.1\%$$

Taking into account close Δb values determined by two independent methods (from positions of the Bragg reflections and from the tilt of the quaterthiophene moieties), one can state that the tilt director is aligned with the lattice vector **b**. The height of crystallites estimated from the angular half-width of the 110 reflection is 19 Å. This is in good agreement with the length of the quaterthiophene units (17 Å).

The results of molecular modelling (Fig. 25) confirm the conclusions drawn after the X-ray study. The model presented here includes the formation of a crystal sublattice in which the quaterthiophene moieties of the same molecule tilted by 14° relative to the substrate surface normal are stacked along the crystallographic vector **b**.

We also studied specific features of collapse of compound **6**. The grazing-incidence X-ray diffraction patterns of such films (Fig. 26) exhibit two sets of reflections denoted by different arrows in the scattering intensity scan. One set of reflections characterizes the quaterthiophene lattice described above. These reflections are relatively weak and broad and their positions coincide with the positions listed in Table 3. The other set includes narrow, relatively strong reflections corresponding to interplanar spacings of 4.25, 3.82 and 3.19 Å. Presumably, they correspond to a similar oligothiophene lattice, but the tilt angle to the substrate surface normal is much larger that in the preceding case. The average film thickness determined by X-ray reflectivity method is 75 Å, which agrees with the molecular length of **6** in the fully extended conformation. Therefore, different sets of reflections correspond to different layers of the material. Namely, molecules in the second, third and subsequent layers are in fact attached to another substrate compared to the molecules in the first layer; therefore, multilayer films quite often form two types of crystallites, one for the bottom layer and the other being characteristic of the remaining layers.

A comparative analysis of multipods based on quaterthiophene showed that perfluorination of a hexyl substituent in dimer **6** (compound **12**) and tetrapod **8** (compound **13**) leads to a considerable shift of the HOMO and LUMO levels relative to the energy levels of unsubstituted

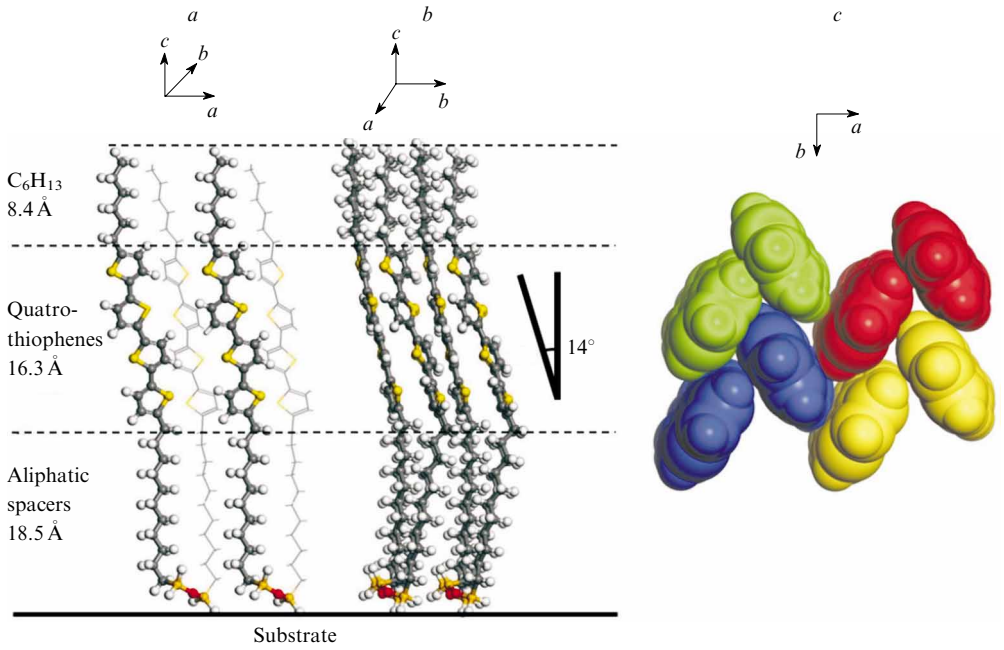


Figure 25. Structure of a monolayer of compound **6** prepared using the LB technique.
Shown are the *ac* (*a*), *bc* (*b*) and *ab* (*c*) projections. In Fig. *c*, the identically coloured oligothiophene moieties belong to the same molecule.

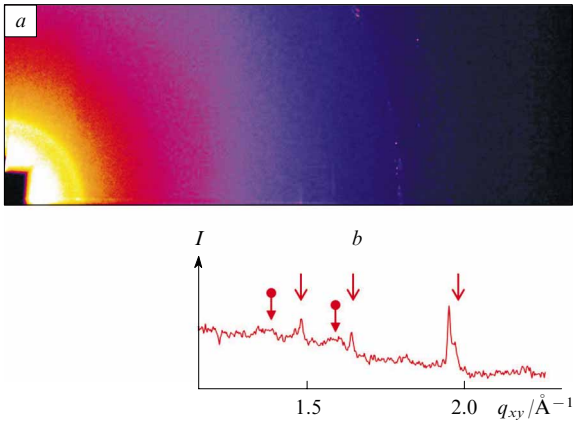


Figure 26. Grazing-incidence X-ray diffraction patterns of Langmuir films of compound **6** prepared on monolayer collapse (*a*) and the diffraction intensity scan along the q_{xy} direction (*b*).

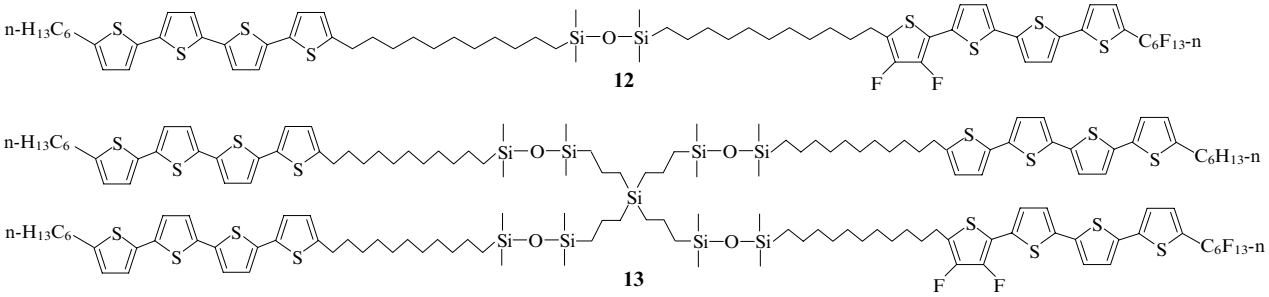
quaterthiophenes; however, the width of the absorption zone remains almost unchanged. Fluorinated compounds are much more stable in atmospheric conditions and form more homogeneous Langmuir layers characterized by higher transfer ratio.

Samples of dimer **12** exist in ordered smectic mesophase with an interlayer spacing of 79.1 Å (Fig. 27), which agrees with the length of the molecule in the fully extended conformation. It should be emphasized that specific electron density distribution within a layer, *viz.*, close values of the separation between the oligothiophene blocks in the same molecule and the spacing between the oligothiophene blocks in neighbouring molecules, leads to a characteristic intensity ratio of the first-to-second-order reflections:

$$\frac{I_2}{I_1} = 52 \gg 1$$

One can assume that the structure of the smectic mesophase formed by compound **12** matches the structure formed by compound **6**.

Structures 12, 13



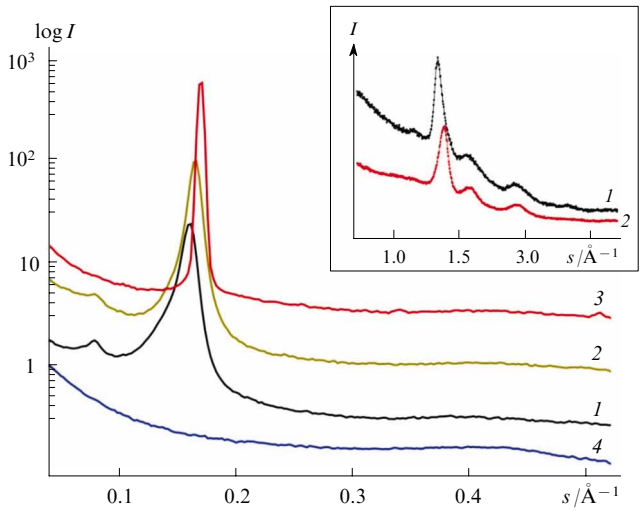


Figure 27. Small-angle X-ray scattering patterns of a sample of compound **12** at 23 (*1*), 80 (*2*), 120 (*3*) and 160 °C (*4*).
Inset: wide-angle X-ray scattering patterns at 23 °C of the samples 12 (*1*) and 13 (*2*).

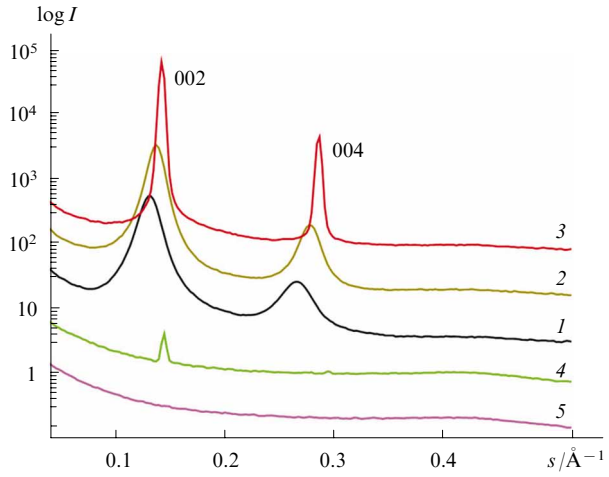


Figure 28. Small-angle X-ray scattering patterns of a sample of compound **13** at 23 (*1*), 100 (*2*), 140 (*3*), 160 (*4*) and 180 °C (*5*).

At room temperature, the wide-angle X-ray scattering patterns of the samples of dimer **12** exhibit a specific group of three reflections characteristic of the crystal packing of oligothiophene (see inset in Fig. 27). This indicates the presence of ordered sublayers (oigothiophene crystallites) in the smectic mesophase of the material.

An increase in temperature is accompanied by rearrangements in the layered structure, which manifests itself as an increase in the intensity of the 002 reflection and simultaneous weakening of the 001 reflection until disappearance at 100 °C. The interlayer distance decreases to 74.8 Å at 100 °C (corresponding thermal expansion coefficient is $\beta = -7.2 \times 10^{-4}$ K^{-1}). Besides, heating of the samples is accompanied by narrowing of crystallographic reflections due to an increase in the size of coherent scattering domains ($L_{002} = 400$ Å in the freshly prepared samples and $L_{002} = 650$ Å at 100 °C). At 120 °C, an abrupt narrowing of the 002 crystallographic reflection ($L_{002} = 950$ Å) is observed; this probably corresponds to the first phase transition in the DSC thermograms. One can assume violation of intra-layer ordering in the smectic phase at this temperature.

Usually, the order–disorder transition within supramolecular aggregates is followed by an abrupt increase in the size of coherent scattering domains, because order within each aggregate (layer) does not correlate with the order within the neighbouring aggregate, which leads to considerable diffusion of the 00*l* reflections. In the disordered smectic mesophase the interplanar crystallographic reflections are due to periodic variations of the electron density along the layer director; their correlations decay weakly with the distance. The temperature behaviour of the samples of dimer **12** is shown in Fig. 27. Isotropization of the compound is observed at 140 °C. According to DSC and X-ray studies, phase transformations in the material are reversible.

Compounds **12** and **13** exhibit qualitatively similar temperature behaviour (see Fig. 27 and Fig. 28, respectively). The small-angle X-ray scattering patterns of freshly prepared samples of the tetramer exhibit the 002 and 004 reflections corresponding to an interplanar spacing 47.0 Å. At room temperature, the wide-angle X-ray scattering patterns of the samples of dimer **12** exhibit a specific group of three reflections, characteristic of the crystal packing of oligothiophene. Heating of the material leads to densification of the smectic packing and to contraction of the interplanar spacing to $D_{002} = 44.1$ Å at 120 °C ($\beta = -6.2 \times 10^{-4}$ K^{-1}) (Fig. 29). The intra-layer order–disorder transition occurs at 140 °C, being followed by isotropization of the samples at 160 °C. The phase transformations of both compounds, **12** and **13**, are reversible.

X-Ray reflectivity studies (Fig. 30) showed that transfer of the LB films of dimer **12** at a transfer pressure of 24 mN m^{-1} leads to formation of well-defined homogeneous layers with a thickness of 39.8 Å, which corresponds to half the length of the molecule. At a higher transfer pressure (35 mN m^{-1}), the layer thickness remains almost unchanged. At the same time, modulation features indicating the formation of polylayers appear in the reflectivity curve whose overall shape varies insignificantly. Such a

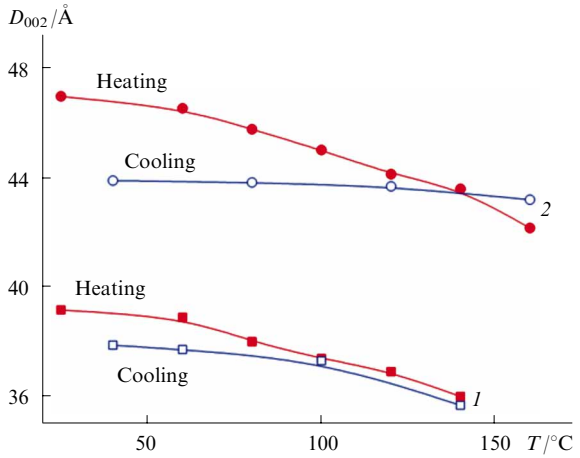


Figure 29. Interlayer distance D_{002} plotted *vs.* temperature for samples of compounds **12** (*1*) and **13** (*2*).

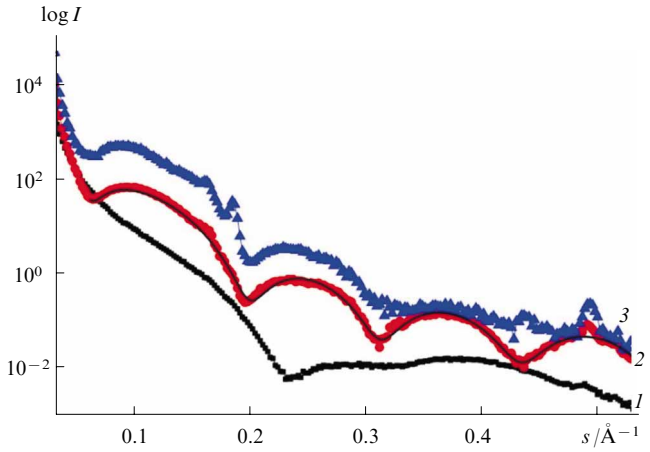


Figure 30. Reflectivity curves of LB films of compound **12** prepared at a surface pressure of 14 (*1*), 24 (*2*) and 35 mN m^{-1} (*3*). For convenience, curves *2* and *3* are shifted along the ordinate axis. The thin black line is the plot of the reconstructed electron density along the normal to the substrate surface.

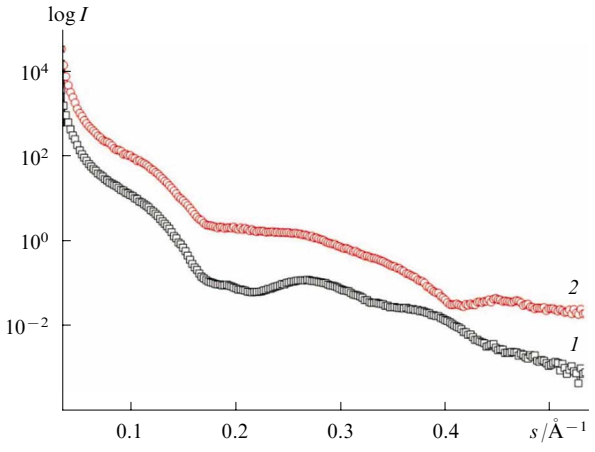


Figure 32. Reflectivity curves of LB films of tetramer **13** prepared at a surface pressure of 14 (*1*) and 35 mN m^{-1} (*2*). For convenience, curve *2* is shifted along the ordinate axis.

polylayer is 5–6 monolayers thick, as evaluated from the width of the modulation features.

The reconstructed electron density distribution along the direction perpendicular to the substrate surface for films of compound **12** prepared at a surface pressure 24 mN m^{-1} (Fig. 31) agrees with the distribution obtained by molecular modelling. Unfortunately, a relatively high electron density on fluorinated hexyl terminal groups precludes resolution of the oligothiophene moieties and the most distant from the substrate aliphatic periphery. However, the averaged calculated electron density value is in good agreement with the experimental value. At the same time, it should be noted that the total electron density, for which the best agreement between calculated and experimental reflectivity curves was observed, is several times higher than the total electron density calculated from the surface area of the unit cell per molecule and the layer thickness. This is probably due to inhomogeneity of the coating on the substrate surface. Calculations performed with inclusion of this discrepancy gave a 40% coverage.

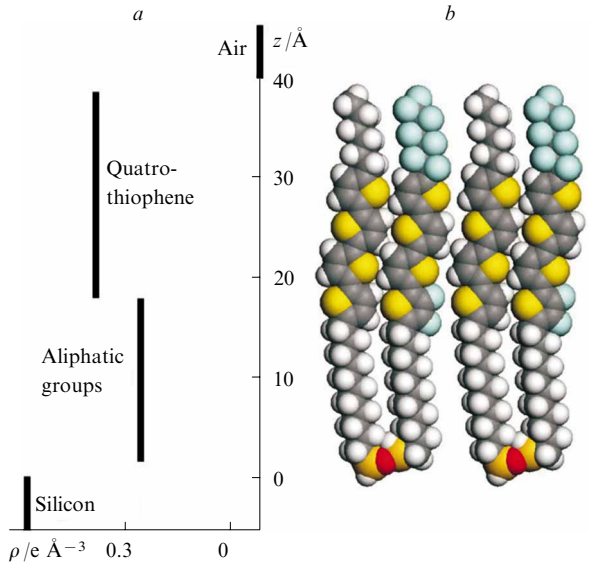


Figure 31. Reconstructed electron density distribution along the substrate surface normal for LB films of dimer **12** at a surface pressure of 24 mN m^{-1} (*a*) and the molecular model for the layer constructed using the same length scale (*b*).

Yet another characteristic feature of compound **13** consists in formation of monolayers with a height of 42.4 Å (Fig. 32). An increase in the film thickness corresponds to an extra siloxane spacer in tetramer **13** compared to dimer **12**. The substrate coverage by the material is also low (~45%). At the same time, no formation of a polylayer structure was observed for samples of the tetramer.

The aforesaid suggests that compounds based on quaterthiophene with different structures form homogeneous layers in which the oligothiophene moieties form a herringbone sublattice owing to π–π interaction between neighbouring units. Sufficiently long aliphatic spacers ensure the possibility of accommodation of oligothiophene blocks in the crystal lattice even if the multipod molecule is attached to the substrate surface in some arbitrary manner. However, it should be noted that the structure of thin films is significantly influenced by the film preparation procedure.

* * *

Summing up, the X-ray methods of investigation considered in this review are nondestructive and do not require special preparation. They are used to obtain valuable and versatile information on specific features of the morphology and quality of the surface of thin films and on structure formation in them. This, in turn, serves as methodological basis for new approaches aimed at optimizing the structure and improving the efficiency of thin-film electronics devices. Further progress in X-ray materials science is associated with utilization of modern sources of synchrotron radiation and high-performance computational facilities to elucidate the 3D structure of materials including synchrotron X-ray

computer tomography, synchrotron X-ray computed laminography and microfocus computed tomography.

This review has been written with the financial support from the Russian Foundation for Basic Research (Project No. 14-13-01402).

References

1. M V Kovalchuk, V V Klechkovskaya, L A Feigin *Priroda* (11) 11 (2003)
2. P Dynarowicz-Latka, A Dhanabalan, O N Oliveira Jr *Adv. Colloid Interface Sci.* **91** 221 (2001)
3. L M Blinov *Sov. Phys. Usp.* **31** 623 (1988) [*Usp. Fiz. Nauk* **155** 443 (1988)]
4. L M Blinov *Russ. Chem. Rev.* **52** 713 (1983)
5. J J Giner-Casares, G Brezesinski, H Möhwald *Curr. Opin. Colloid Interface Sci.* **19** 176 (2014)
6. W D Harkins, T Fraser Yg, E Boyd *J. Chem. Phys.* **8** 954 (1940)
7. A W Adamson, A P Gast *Physical Chemistry of Surfaces* (Chichester: Wiley, 1997)
8. D J Crisp, in *Surface Phenomena in Chemistry and Biology* (Eds J F Danielli, K G A Pankhurst, A C Riddiford) (New York: Pergamon Press, 1958)
9. D J Kuzmenka, S Granick *Macromolecules* **21** 779 (1988)
10. A. M. Yashchenok, D A Gorin, K E Pankin, M V Lomova, S N Shtykov, B N Klimov, G I Kurochkina, M K Grachev *Semiconductors* **41** 684 (2007) [*Fiz. Tekh. Poluprovod.* **41** 706 (2007)]
11. G Binnig, H Rohrer, Ch Gerber, E Weibel *Phys. Rev. Lett.* **49** 57 (1982)
12. G Binnig, C F Quate, Ch Gerber *Phys. Rev. Lett.* **56** 930 (1986)
13. G Friedbacher, H Fuchs *Pure Appl. Chem.* **71** 1337 (1999)
14. H K Wickramasinghe *Acta Mater.* **48** 347 (2000)
15. M A Poggi, L A Bottomley, P T Lillehei *Anal. Chem.* **74** 2851 (2002)
16. T R Albrecht, P Grütter, D Horne, D Rugar *J. Appl. Phys.* **69** 668 (1991)
17. S N Magonov, D H Reneker *Ann. Rev. Mater. Sci.* **27** 175 (1997)
18. S S Sheiko, M Möller *Chem. Rev.* **101** 4099 (2001)
19. *Surface Analysis with STM and AFM* (Eds S N Magonov, M-H Whangbo) (Weinheim: VCH, 1996)
20. J R Hahn, H Kang, S Song, I C Jeon *Phys. Rev.* **53** 1725 (1996)
21. S Kopta, M Salmeron *J. Chem. Phys.* **113** 8249 (2000)
22. O Sahin, N Erina *Nanotechnology* **19** 445717 (2008)
23. H Dosch, B W Batterman, D C Wack *Phys. Rev. Lett.* **56** 1144 (1986)
24. H Dosch *Phys. Rev. Lett. B* **35** 2137 (1987)
25. L G Parratt *Phys. Rev.* **95** 359 (1954)
26. H Kiessig *Annal. Phys.* **10** 769 (1931)
27. S Fisk, B Widom *J. Chem. Phys.* **50** 3219 (1969)
28. K Binder *J. Chem. Phys.* **79** 6387 (1983)
29. D Broseta, G H Fredrickson, E Helfand, L Leibler *Macromolecules* **23** 132 (1990)
30. E Helfand, S M Bhattacharjee, G H Fredrickson *J. Chem. Phys.* **91** 7200 (1972)
31. D W Schubert, M Stamm *Europhys. Lett.* **35** 419 (1996)
32. H Tang, K F Freed *J. Chem. Phys.* **94** 6307 (1991)
33. J Als-Nielsen *Structure and Dynamics of Surfaces (Topics in Current Physics* Vol. 2) (Berlin, Heidelberg: Springer, 1986)
34. J Als-Nielsen, D Jacquemain, K Kjær, F Leveiller, M Lahav *Phys. Rep.* **246** 251 (1994)
35. P S Pershan *Faraday Discuss Chem. Soc.* **89** 231 (1990)
36. S Banerjee, M K Sanyal, A Datta, S Kanakaraju, S Mohan *Phys. Rev. B* **54** 16377 (1996)
37. M K Sanyal, J K Basu, A Datta, S Banerjee *Europhys. Lett.* **36** 265 (1996)
38. A K Doerr, M Tolan, T Seydel, W Press *Physica B* **248** 263 (1998)
39. W L Clinton *Phys. Rev. B* **48** 1 (1993)
40. G Reiss *Physica B* **221** 533 (1996)
41. M V Kovalchuk, V G Kohn *Sov. Phys. Usp.* **29** 426 (1986) [*Usp. Fiz. Nauk* **149** 69 (1986)]
42. M V Kovalchuk, A Yu Kasimirov, S I Zheludeva *Nucl. Instr. Methods B* **101** 435 (1995)
43. J Bedsyk, G Materlik, M V Kovalchuk *Phys. Rev.* **30** 2453 (1984)
44. S I Zheludeva, B G Zakharov, M V Kovalchuk, V G Kohn, E A Sozontov, A N Sosphenov *Kristallografiya* **33** 1352 (1988) [a]
45. A Yu Kasimirov, M V Kovalchuk, A N Sosphenov, V G Kohn, J Kub, P Novak, M Nevriva, J Germak *Acta Crystallogr. B* **48** 577 (1992)
46. M V Kovalchuk, A Ya Kreynes, Yu A Osip'yan, V V Kvardakov, V A Somenkov *J. Exp. Theor. Phys. Lett.* **65** 734 (1997) [*Pis'ma Zh. Eksp. Teor. Fiz.* **65** 703 (1997)]
47. G Borrmann *Z. Phys.* **42** 157 (1941)
48. G Borrmann *Z. Phys.* **127** 297 (1950)
49. M Renninger *Adv. X-Ray Anal.* **10** 32 (1967)
50. R Bubakova, J Drahokoupil, A Fingerland *Czech. J. Phys., Ser. B* **12** 538 (1982)
51. R Bubakova, J Drahokoupil, A Fingerland *Czech. J. Phys., Ser. B* **12** 764 (1982)
52. W H Zachariasen *Theory of X-Ray Diffraction in Crystals* (New York: Wiley, 1945)
53. R W James *The Optical Principles of The Diffraction of X Rays* (London: G Bell and Sons, 1948)
54. M Laue *Röntgenstrahlinterferenzen* (Frankfurt am Main: Akademische Verlag, 1960)
55. Z G Pinsker *Dynamical Scattering of X-Rays in Crystals* (Heidelberg, New York: Springer, 1978)
56. Z G Pinsker *Rentgenovskaya Kristallooptika* (X-Ray Crystal Optics) (Moscow: Nauka, 1982)
57. P L Cowan, J A Golovchenko, M F Robbins *Phys. Rev. Lett.* **44** 1680 (1980)
58. T Vuorinen, K Kaunisto, N V Tkachenko, A Efimov, H Lemmetyinen, A S Alekseev, K Hosomizu, H Imahori *Langmuir* **21** 5383 (2005)
59. A Yu Seregin, Yu A Dyakova, S N Yakunin, I A Makhotkin, A S Alekseev, V V Klechkovskaya, E Yu Tereschenko, N V Tkachenko, H Lemmetyinen, L A Feigin, M V Kovalchuk *Cryst. Rep.* **58** 934 (2013) [*Kristallografiya* **58** 940 (2013)]
60. V V Roddatis, S N Yakunin, A L Vasiliev, M V Kovalchuk, A Yu Seregin, T M Burbaev, M N Gordeev *J. Mat. Res.* **28** 1432 (2013)
61. J Roncali, P Leriche, A Cravino *Adv. Mater.* **19** 2045 (2007)
62. I F Perepichka, D F Perepichka, H Meng, F Wudl *Adv. Mater.* **17** 2281 (2005)
63. U Scherf, E J W List *Adv. Mater.* **14** 477 (2002)
64. J Roncali *Macromol. Rapid Commun.* **28** 1761 (2007)
65. G Horowitz *Adv. Mater.* **10** 923 (1998)
66. B Pepin Donat, S Panozzo, J-C Vial, C Beigne, F Rieutord *Synth. Met.* **146** 225 (2004)
67. I McCulloch, C Bailey, M Giles, M Heeney, I Love, M Shkunov, D Sparrowe, S Tierney *Chem. Mater.* **17** 1381 (2005)
68. A R Murphy, J Liu, C Luscombe, D Kavulak, J M J Frechet, R J Kline, M D McGehee *Chem. Mater.* **17** 4892 (2005)
69. T Yamamoto, H Kokudo, M Kobashi, Y Sakai *Chem. Mater.* **16** 4616 (2004)
70. J Matsui, S Yoshida, T Mikayama, A Aoki, T Miyashita *Langmuir* **21** 5343 (2005)
71. H G O Sandberg, G L Frey, M N Shkunov, H Sirringhaus, R H Friend *Langmuir* **18** 10176 (2002)
72. A G MacDiarmid *Angew. Chem., Int. Ed.* **40** 2581 (2001)

73. A G Heeger *Angew. Chem., Int. Ed.* **40** 2591 (2001)
74. H Shirakawa *Angew. Chem., Int. Ed.* **40** 2574 (2001)
75. A Mishra, C-Q Ma, P Biuerle *Chem. Rev.* **109** 1141 (2009)
76. S Kirchmeyer, K Reuter *J. Mater. Chem.* **15** 2077 (2005)
77. K Reuter, S Kirchmeyer, A Elschner, in *Handbook of Thiophene-Based Materials: Applications in Organic Electronics and Photonics* Vol. 2 (Eds I F Perepichka, D F Perepichka) (Chichester: Wiley, 2009) p. 549
78. P C Ewbank, M C Stefan, G Sauvé, R D McCullough, in *Handbook of Thiophene-Based Materials: Applications in Organic Electronics and Photonics* Vol. 1 (Eds I F Perepichka, D F Perepichka) (Chichester: Wiley, 2009) p. 157
79. C D Dimitrakopoulos, A R Brown, A Pomp *J. Appl. Phys.* **80** 2501 (1996)
80. C Tanase, E J Meijer, P W M Blom, D M de Leeuw *Org. Electronics* **4** 33 (2003)
81. F Dinelli, M Murgia, P Levy, M Cavallini, F Biscarini *Phys. Rev. Lett.* **92** 116802 (2004)
82. D V Anokhin, M Defaux, A Mourran, M Moeller, Yu N Luponosov, O V Borshchev, A V Bakirov, M A Shcherbina, S N Chvalun, T Meyer-Friedrichsen, A Elschner, S Kirchmeyer, S A Ponomarenko, D A Ivanov *J. Phys. Chem. C* **116** 22727 (2012)
83. G Ungar *Polymer* **34** 2050 (1993)
84. M Defaux, L Vidal, M Moeller, R Gearba, E Dimasi, D A Ivanov *Macromolecules* **42** 3500 (2009)
85. R I Gearba, D V Anokhin, A I Bondar, Yu K Godovsky, V S Papkov, N N Makarova, S N Magonov, W Bras, M H J Koch, F Masin, B Goderis, D A Ivanov *Macromolecules* **39** 988 (2006)
86. T Siegrist, C Kloc, R A Laudise, H E Katz, R C Haddon *Adv. Mater.* **10** 379 (1998)
87. S Ponomarenko, S J Kirchmeyer *Mater. Chem.* **13** 197 (2003)
88. S A Ponomarenko, O V Borshchev, S Setayesh, E C P Smits, S G J Mathijssen, A P Pleshkova, T Meyer-Friedrichsen, S Kirchmeyer, A M Muzafarov, D M de Leeuw *Organometallics* **29** 4213 (2010)
89. E V Agina, I A Usov, O V Borshchev, J Wang, A Mourran, M A Shcherbina, A V Bakirov, S Grigorian, M Möller, S N Chvalun, S A Ponomarenko *Langmuir* **28** 16186 (2012)
90. A Mourran, B Tartsch, M Gallyamov, S Magonov, D Lambreva, B I Ostrovskii, I P Dolbnya, W H de Jeu, M Moeller *Langmuir* **21** 2308 (2005)
91. M Björck, G Andersson *J. Appl. Cryst.* **40** 1174 (2007)
92. E J Samuelsen, J Mardalen, in *Handbook of Conductive Molecules and Polymers: Conductive Polymers: Spectroscopy and Physical Properties* Vol. 3 (Ed. H S Nalwa) (London: Wiley, 1997)

[a] — *Crystallograph. Rep. (Engl. Transl.)*